



Formation and degradation of a porphyry occurrence: The Oligocene Khatoon-Abad porphyry Mo-Cu system, NW Iran

Ahmad Rabiee^{a,*}, Federico Rossetti^a, Michele Lustrino^b, Hossein Azizi^c, Yoshihiro Asahara^d, Saeed Alipour^e, David Selby^f

^a Dipartimento di Scienze, Università degli Studi Roma Tre, Roma, Italy

^b Dipartimento di Scienze della Terra, Sapienza Università di Roma, Roma, Italy

^c Department of Mining, Faculty of Engineering, University of Kurdistan, Sanandaj, Iran

^d Department of Earth and Environmental Sciences, Nagoya University, Nagoya, Japan

^e Pars Olang Engineering Consultant Co., Tehran, Iran

^f Department of Earth Sciences, Durham University, Durham, UK

ARTICLE INFO

Keywords:

Porphyry Mo-Cu system
U-Pb zircon geochronology
Molybdenite Re-Os geochronology
Degradation
Productive magma
Multiple intrusion
Iran

ABSTRACT

This study investigates the temporal relationships between mineralization and magmatism in the Khatoon-Abad porphyry Mo-Cu deposit (Urumieh-Dokhtar Magmatic Arc, NW Iran). Integrated zircon U-Pb and molybdenite Re-Os dating document a prolonged stationary magmatism, spanning ~ 45 Myr (from ~ 66 to ~ 21 Ma; Paleocene-Early Miocene). Three main Oligocene ore-bearing granitic intrusions and an early Miocene barren dyke swarm are documented, with the main mineralization formed at ~ 27 Ma, as attested by the molybdenite Re-Os age of 26.75 ± 0.14 Ma and the zircon U-Pb age 26.93 ± 0.30 Ma from the host granodiorite porphyry. Despite having similar geochemical fingerprints, including an adakitic signature and having REE patterns similar to productive magmas, the subsequent Oligocene granite bodies (~26.0–25.7 Ma) yielded lower Mo-Cu enrichments and the early Miocene rhyodacite dykes (~21 Ma) are barren. This evidence demonstrates that the efficiency of mineralization has been reduced by changes in the physiochemical conditions of magmatic-hydrothermal systems over time. We suggest that a perturbed geothermal gradient during later Oligocene granite (at ~ 26 Ma) caused slow cooling/degassing of the melts, and hence determined an inefficient mineralization environment. We also infer that during the latest granite porphyry pulse (~25.7 Ma), the structurally-controlled emplacement at shallower levels resulted in rapid melt cooling along with more meteoric water mixing, eventually minor potassic but vast phyllitic alterations, and hence, causing a dispersed mineralization rather than a focused fluid flow. Therefore, the later Oligocene and early Miocene magmatic pulses degraded the early mineralization. The results of this study emphasize that a consistent magma supply into the chamber followed by a rapid magma-fluid flux to the mineralization site are needed for efficient mineralization in collisional settings. Otherwise, multiple mineralization pathways and sites would result in low-grade ore bodies.

1. Introduction

Porphyry Cu ± Mo ± Au deposits commonly form as multi-intrusion complexes, where one or more pulses of productive magmas coexist with less productive or barren ones (Tosdal, 2001; Sillitoe, 2010; Barra et al., 2013; Rabiee et al., 2019; Yang and Zhang, 2021). In this regard, multiple magma batches may enhance or degrade the early-stage ore bodies (e.g., Sillitoe, 2010; Vry et al., 2010; Xue et al., 2016; Chen et al., 2021). Indeed, changes in the magma emplacement depths, chemistry, and the varying rheological conditions during magma emplacement may

influence fluid chemistry, volumes and flow pathways, and, consequently, the metals transport/deposition capacity through the structurally controlled cupola zones (e.g., Shinohara and Hedenquist, 1997; Cox et al., 2001; Tosdal, 2001; Corbett, 2002; Ulrich and Heinrich, 2002; Sillitoe, 2010; Wilkinson, 2013; Richards, 2021). Moreover, regional tectonics may also perturb the early magmatic-hydrothermal system, causing volcanic eruption, outgassing, and, consequently, incomplete mineralization (Oyarzun et al., 2001; Asadi et al., 2014). Therefore, to decrypt the mineralization history of a porphyry system, it is essential to frame each magma batch in a temporal sequence of events (Chiaradia

* Corresponding author.

E-mail address: ahmad.rabiee@uniroma3.it (A. Rabiee).

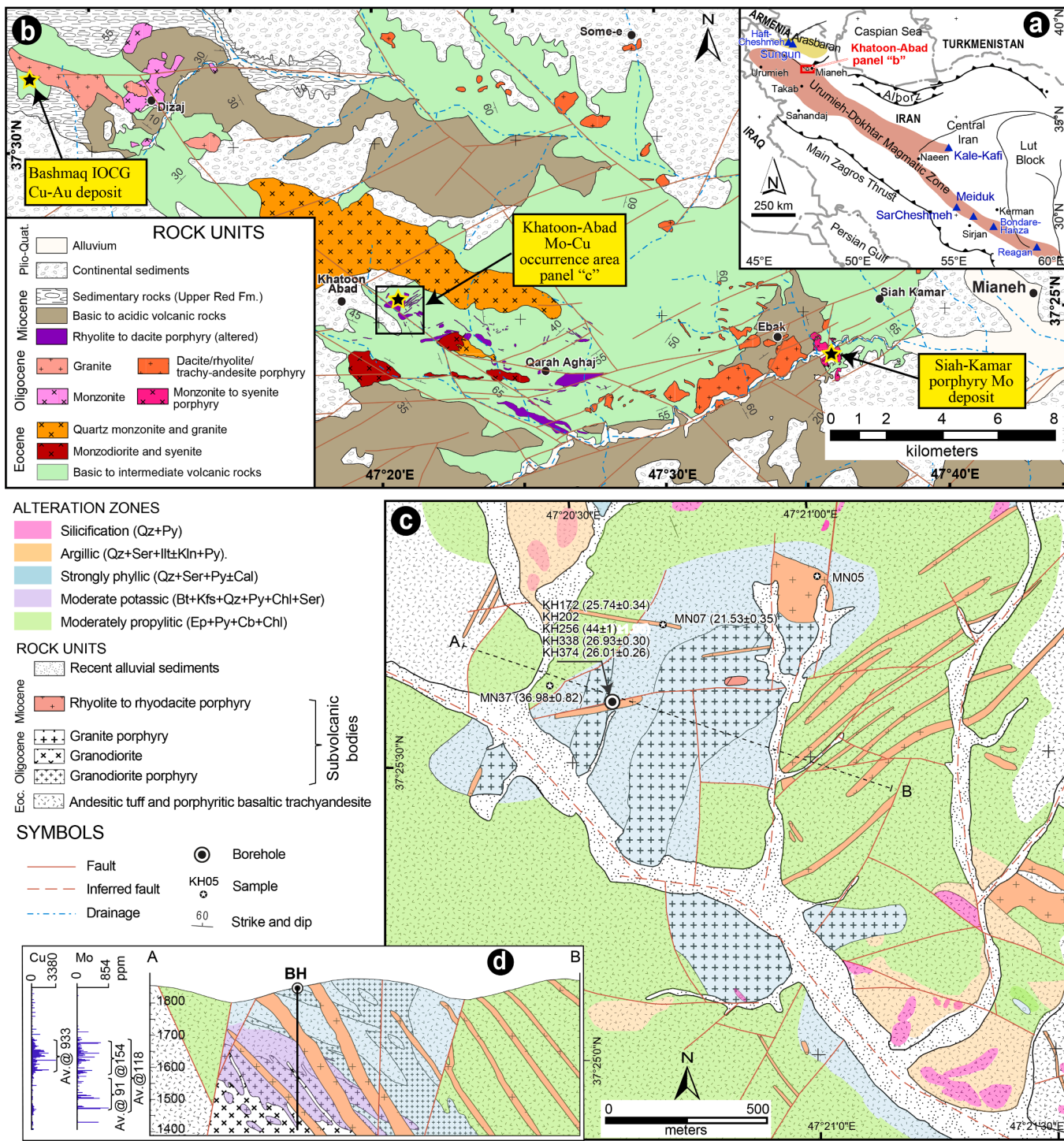


Fig. 1. (a) Index map of Iran showing location of the UDMA and the Khatoon-Abad porphyry Mo-Cu deposit (KHD). (b) Simplified geological map of Mianeh-Hashtroud region (modified after Amidi et al., 1987; NICICO, 2009c; NICICO, 2009b; NICICO, 2009a; Rabiee et al., 2020). (c) Geological-alteration map of the KHD, displaying the distribution of the main alteration types (modified from Rabiee et al., 2020) and sample locations. (d) Conceptual geological cross section showing the distribution of alteration zones in the KHD as obtained from outcrop and borehole core logging information. In addition, the in-depth distribution of the Mo and Cu concentrations is also shown. Abbreviations: Ab, Albite; Bt, Biotite; Cal, Calcite; Cb, Carbonates; Chl, Chlorite; Ep, Epidote; Kln, Kaolinite; Ilt, Illite; Kfs, K-feldspar; Mag, Magnetite; Py, Pyrite; Qz, Quartz; Ser, Sericite.

et al., 2013; Courtney-Davies et al., 2020; Large et al., 2020).

Recent explorations within the Mianeh-Hashtroud metallogenic zone of the Cenozoic Urumieh-Dokhtar magmatic arc (UDMA; Alavi (1994); Fig. 1a) have led to the discovery of the only known porphyry Mo system of Iran (the Siah-Kamar Mo deposit; Nabatian et al., 2017; Rabiee et al., 2019, 2023; Simmonds et al., 2019). A few more geochemically

anomalous zones (of Cu – Mo ± W) have been reported within the Mianeh-Hashtroud metallogenic zone (NICICO, 2009b; Rabiee et al., 2019); among them, the Khatoon-Abad porphyry Cu-Mo deposit (hereafter referred to as KHD) is the most prominent one (Fig. 1b). Preliminary explorations led to drilling some boreholes on the main alteration and geochemically anomalous zones, allowing to define the

Table 1

Petrographic description of the studied samples from the KHD area, with location and ages.

Sample ⁽¹⁾	Coordinates		Age (Ma ± 2σ) ⁽²⁾	Rock Type (TAS) ⁽⁴⁾	Texture	Mineralogy
	Easting	Northing				
Volcanic country rocks (Eocene)						
KH202	47.3428	37.4267	–	Trachy-andesite	Porphyritic-hypohyaline (aphanitic matrix)	Phenocrysts: Pl; Matrix: Pl, glass, Py, glass (mostly altered to Kfs, Bt, Cal, Ser, Chl), Opaques; Accessory Minerals: Ap, Zrn
KH256	47.3428	37.4267	44 ± 1	Andesitic tuff (?)	Secondary minerals	strongly altered to Kfs, Bt, Cal (Qz-Kfs and Cal veins), Opaques; Accessory Minerals: Ap, Zrn.
MN37	47.3427	37.4280	36.98 ± 0.82	Basaltic trachy-andesite	Porphyritic-hypohyaline (Porphyritic – aphanitic matrix)	Phenocrysts: Pl; Matrix: Pl, Cpx, Amp, glass (mostly altered to Epi, Cal, Ser, Chl)
Hypabyssal/Subvolcanic rocks⁽⁴⁾ (Oligocene)						
KH338	47.3428	37.4267	26.93 ± 0.30	Granodiorite	Porphyritic-holocrystalline	Kfs, Pl, Bt, Qz (mostly fractured)
	(Depth: 338 m)					Accessory Minerals: Chl, Py, Ap, Zrn.
KH374	47.3428	37.4267	26.01 ± 0.26	Granite	Equigranular –holocrystalline	Kfs, Pl, Bt, Qz
	(Depth: 372 m)					Accessory Minerals: Py, Cb, TiO ₂ polymorphs, Ap, Zrn.
KH172	47.3428	37.4267	25.74 ± 0.34	Granite	Porphyritic-holocrystalline	Kfs, Pl, Bt, Qz (mostly fractured)
	(Depth: 172 m)					Accessory Minerals: Py, Ap, Zrn.
Hypabyssal/Subvolcanic rocks (Miocene)						
MN05	47.3506	37.4299	22.60 ± 0.41 ⁽³⁾	Rhyolite	Porphyritic-hypohyaline	Phenocrysts: Kfs, Qz, Pl; Matrix: Qz, Kfs, glass
MN07	47.3447	37.4288	21.53 ± 0.35	Rhyodacite	Porphyritic-hypohyaline	Accessory Minerals: Ap, Zrn
						Phenocrysts: Pl; Matrix: Pl, Qz, Opaques, glass
						Accessory Minerals: Ap, Zrn

⁽¹⁾ Sample with prefix "KH" are from the borehole and the following number stand for the depth ⁽²⁾ U-Pb zircon ages (this study); ⁽³⁾ after Rabiee et al. (2019); ⁽⁴⁾ For the intrusive rocks the nomenclature is after Middlemost (1994). Abbreviations: Ab, Albite; Amp, Amphibole; Ap, Apatite; Bt, Biotite, Cpx, Clinopyroxene; Cal, Calcite; Cb, Carbonates; Chl, Chlorite; Ep, Epidote; Kln, Kaolinite; Ilt, Illite; Kfs, K-feldspar; Mag, Magnetite; Pl, Plagioclase; Py, Pyrite; Qz, Quartz; Ser, Sericite; Zrn, Zircon.

in-depth distribution of the ore bodies and the associated magmatism.

This contribution aims at characterizing the geochronology and mineralization potential of the KHD in the framework of the Cenozoic collisional setting of the UDMA. We provide new field data, integrated with petrographic investigation, whole-rock geochemical data of the outcropping and borehole magmatic rocks samples, and the in-depth Mo and Cu elemental distribution. The geochronological framework of mineralization is constrained through zircon U-Pb dating of the main magmatic rock types together with molybdenite Re-Os dating of the main ore body. The KHD provides a case study where the episodic incremental magma emplacement during Oligocene-Early Miocene reduced the mineralization capability at the mineralization site, with the effect of degrading the economic potential of the early Mo ore body over time. Inferences on the controlling factors leading to ore enhancement/degradation of the mineralization systems are discussed in the framework of the regional collisional setting.

2. Geological background

The UDMA is a major Cenozoic NW-SE trending magmatic zone located in the hinterland of the Alpine Arabia-Eurasia convergence zone (Fig. 1a). It hosts some of the outstanding giant Cu-Mo-Au porphyry systems in Iran (e.g., Shahabpour and Kramers, 1987; Shafiei et al., 2008; Taghipour et al., 2008; Asadi et al., 2014, 2018; Aghazadeh et al., 2015). The porphyry/epithermal mineralization within the UDMA began in Eocene (e.g., Moritz et al., 2006; Siani et al., 2015; Ahmadian et al., 2016; Karimpour et al., 2017), and continued in Oligocene, during ~ 33–26 Ma (e.g., Reagan, Hassanzadeh, 1993; Haftcheshmeh, Bondar-e Hanza, Aghazadeh et al., 2015). Mineralization enhanced during the early Miocene in Arasbaran (e.g., Sungun, ~ 23–19 Ma, Hassanzadeh et al., 2014) and the middle Miocene in the southern UDMA (e.g., SarCheshmeh; Shahabpour and Kramers, 1987), a time lapse correlating well with the major collisional phases along the Zagros

convergence zone (Shafiei et al., 2009; Asadi et al., 2014, 2018; Rabiee et al., 2022). Indeed, the styles and distribution of the Cenozoic porphyry mineralization vary significantly along the UDMA due to the changing magma chemistry, being primarily focused along the major inherited crustal/lithosphere anisotropies and controlled by the dynamics of continental collision and associated mantle processes (e.g., Hou et al., 2009; Asadi et al., 2014; Rabiee et al., 2022; Babazadeh et al., 2024a; Babazadeh et al., 2024b).

Within this context, the Mianeh-Hashtroud magmatic zone of the UDMA documents a long-lived magmatic activity, spanning Eocene-Miocene times (from ~ 45 to ~ 21 Ma; Rabiee et al., 2020). The region hosts the only porphyry Mo deposit in Iran, the Siah-Kamar porphyry Mo deposit (Nabatian et al., 2017; Rabiee et al., 2019; 2023; Simmonds et al., 2019). This Mo ore is associated with the Oligocene age Bashmagh-Ghazikandi IOCG (Iron Oxide Cu-Au) deposit (Sohrabi and Rezaei Aghdam, 2016) that occurs in the western part of the Mianeh-Hashtroud magmatic zone (Fig. 1b). In the Siah-Kamar Mo deposit, the early stage high-temperature and disseminated Mo mineralization formed at ~ 33–32 Ma (U-Pb zircon and Rb-Sr multimineral geochronology) associated with a micro quartz monzodiorite porphyry, overprinted by a carbonatization stage during the high-grade ore formation at ~ 29–28 Ma (Rabiee et al., 2023) following injection of rhyodacite porphyry dykes. The Bashmagh-Ghazikandi IOCG deposit constitutes the peripheral zone of a granular granitic stock emplaced at 28.4 ± 0.9 Ma (U-Pb zircon age; Rabiee et al., 2020; Fig. 1b) in the Eocene country rocks.

The KHD is a porphyry Cu-Mo system that occurs within the central part of the Mianeh-Hashtroud magmatic zone. The regional stratigraphy is characterized by vast outcrops of mainly intermediate to acidic Eocene volcano-plutonic rocks, forming the country rocks of the KHD (Amidi et al., 1987; Fig. 1 b). A suite of Oligocene-Miocene stocks and dykes, encompassing compositions, spanning from diorite, monzonite to granite, and rhyodacite to rhyolite, with a general porphyritic texture

Table 2

Whole-rock chemical composition of the magmatic rock samples from the KHD (*).

Rocks	Eocene country rocks			Oligocene subvolcanics					Miocene dyke	
Samples	KH256	KH202	MN37	KH338-1	KH338-2	KH372-5	KH372-6	KH172	MN05	MN07
Major oxides (wt.%)										
SiO ₂	53.63	51.64	54.27	66.32	64.89	66.25	66.00	65.33	77.97	67.11
TiO ₂	0.76	0.83	0.84	0.47	0.58	0.35	0.41	0.46	0.11	0.71
Al ₂ O ₃	14.12	16.52	18.83	15.77	15.92	15.12	13.68	14.67	10.57	16.99
Fe ₂ O _{3(t)}	8.69	8.15	6.28	3.56	3.96	3.04	3.79	4.14	0.75	3.22
MnO	0.20	0.16	0.12	0.10	0.09	0.08	0.10	0.09	0.01	0.00
MgO	4.86	2.14	2.12	1.28	1.66	1.13	1.36	1.88	0.12	0.48
CaO	3.96	3.29	5.59	3.02	2.60	2.70	2.43	2.51	0.14	0.30
Na ₂ O	0.86	6.42	3.27	5.02	4.67	4.20	3.87	1.56	3.40	2.56
K ₂ O	3.96	3.33	5.16	2.66	2.07	4.14	4.35	5.43	3.44	4.68
P ₂ O ₅	0.28	0.36	0.64	0.19	0.30	0.14	0.16	0.21	0.01	0.13
LOI	8.40	7.15	1.98	1.49	2.55	2.74	3.78	3.71	0.66	4.18
Total	99.72	99.99	99.10	99.88	99.29	99.89	99.93	99.99	97.18	100.36
Mg#*	0.58	0.39	0.46	0.47	0.51	0.48	0.47	0.53	0.29	0.27
A/CNK	1.09	0.82	0.89	0.95	1.09	0.93	0.88	1.10	1.73	1.13
Large-ion lithophile element (LILE)										
Cs	22.5	2.7	4.8	6.8	7.5	4.9	2.4	9.1	1.2	3.8
Rb	244	158	136	120	137	156	156	204	102	170
Ba	625	365	1018	527	410	587	597	708	150	890
Sr	372	619	759	487	525	470	377	231	49	403
Pb	83	228	136	185	64	2543	609	30	102	170
High field-strength elements (HFSE)										
Th	6.47	6.47	9.70	8.41	12.5	16.6	11.6	14.1	35.3	10.9
U	1.1	1.4	3.2	2.6	2.6	6.3	9.3	10.7	5.9	3.6
Zr	11	23	136	16	16	12	7	19	71	276
Hf	–	–	3.97	–	–	–	–	1.30	3.54	5.80
Ta	0.54	0.48	0.62	0.47	1.01	0.87	0.94	1.30	2.26	0.99
Y	18.0	16.0	22.6	9.3	11.2	9.6	12.4	9.3	8.6	27.4
Nb	6.0	6.9	9.2	12.0	23.2	12.3	15.8	15.4	28.4	23.5
Rare earth elements (REE)										
La	26.0	22.0	37.8	37.0	37.0	29.0	33.0	33.0	32.4	39.6
Ce	50.0	45.0	71.1	61.0	66.0	50.0	57.0	57.0	49.5	76.8
Pr	6.57	5.94	8.28	6.07	6.86	5.12	5.09	6.25	4.23	8.89
Nd	29.2	25.6	31.6	21.2	25.0	18.4	17.9	22.7	11.6	33.4
Sm	6.28	4.61	5.92	2.73	3.39	3.01	3.42	3.80	1.75	6.53
Eu	1.56	1.22	1.56	0.93	0.94	1.16	0.90	1.25	0.16	1.26
Gd	4.50	3.80	5.39	3.18	3.61	2.63	1.93	3.56	1.33	5.36
Tb	0.60	0.60	0.75	0.39	0.44	0.41	0.26	0.40	0.20	0.73
Dy	3.94	4.05	4.45	2.30	2.55	2.39	1.84	2.70	1.28	4.50
Er	1.70	1.93	2.42	0.82	0.96	0.83	0.95	1.20	1.00	2.93
Tm	0.18	0.22	0.37	0.05	0.14	0.10	0.13	0.20	0.20	0.46
Yb	1.60	1.40	2.33	0.40	0.50	0.60	0.90	0.82	1.49	3.00
Lu	0.19	0.13	0.40	0.12	0.13	0.14	0.14	0.20	0.24	0.50
Sr/Y	20.7	38.7	33.5	52.4	46.9	49.0	30.4	24.8	5.7	14.7
(La/Yb) _N	11.7	11.3	11.7	66.4	53.1	34.7	26.3	118.4	15.6	9.45
(Dy/Yb) _N	1.58	1.85	1.23	3.68	3.27	2.55	1.31	8.65	0.55	0.96
Eu/Eu [*]	0.90	0.89	0.85	0.96	0.82	1.26	1.07	1.03	0.32	0.64
Other elements										
Sc	18.2	19.3	11.9	4.7	6.3	4.6	5.7	6.8	0.9	10.7
Cr	34	25	24	22	18	19	27	20	201	26
Ni	47	9	16	16	9	12	13	11	103	13
Co	28	15.6	11.7	6.8	8.2	9.4	5.8	9.9	3.2	0.7
V	219	118	139	74	83	59	70	84	10.8	57.4
W	7.3	21	–	2.4	28	120	34	14	4.3	244
Zn	96	94	178	35	57	45	145	34	60	21
Cu	660	835	39	304	98	325	383	252	40	54

(*): LOI, mass loss on ignition; “–“: Not measured; A/CNK – molar [Al₂O₃/(CaO + Na₂O + K₂O)]; Mg#, (MgO / 40.31) / ((MgO / 40.31) + (Fe₂O_{3tot}/(Fe₂O_{3tot} × 0.20)) × 0.8998 / 71.85); Eu/Eu^{*}, Eu_N × [Sm_N × Gd_N]^{1/2} (Taylor and McLennan, 1985) where the subscript ‘N’ denotes CI chondrite-normalised values after Sun and McDonough (1989); Samples with prefix “MN” are from Rabiee et al. (2020).

(Amidi et al., 1987; Khodabandeh et al., 1999; Rabiee et al., 2020), are intruded within the Eocene country rocks (Amidi et al., 1987; Khodabandeh et al., 1999). The early Miocene volcanic rocks mainly consist of andesitic lava beds, cropping out in the southern sector of the region, whereas late Miocene tuff and ash layers with interlayered andesitic lava beds are observed in the northern part of the study area (Fig. 1b). The late Miocene continental (Upper Red Fm.) and Pliocene-Quaternary sedimentary deposits unconformably cover the magmatic products (Amidi et al., 1978; Ballato et al., 2017; Ghorbani, 2021). Some of the Oligocene stocks are associated with remarkable alteration zones,

hosting significant Cu-Mo (± W) geochemical anomalies (Rabiee et al., 2019).

3. Materials and methods

The geological characterisation of the KHD was achieved through and integrated research approach, which combines fieldwork with petrographic, geochemical and geochronological investigations.

Fieldwork was based on the 1:250,000 scale geological maps (Amidi et al., 1987; Khodabandeh et al., 1999), integrated with data provided

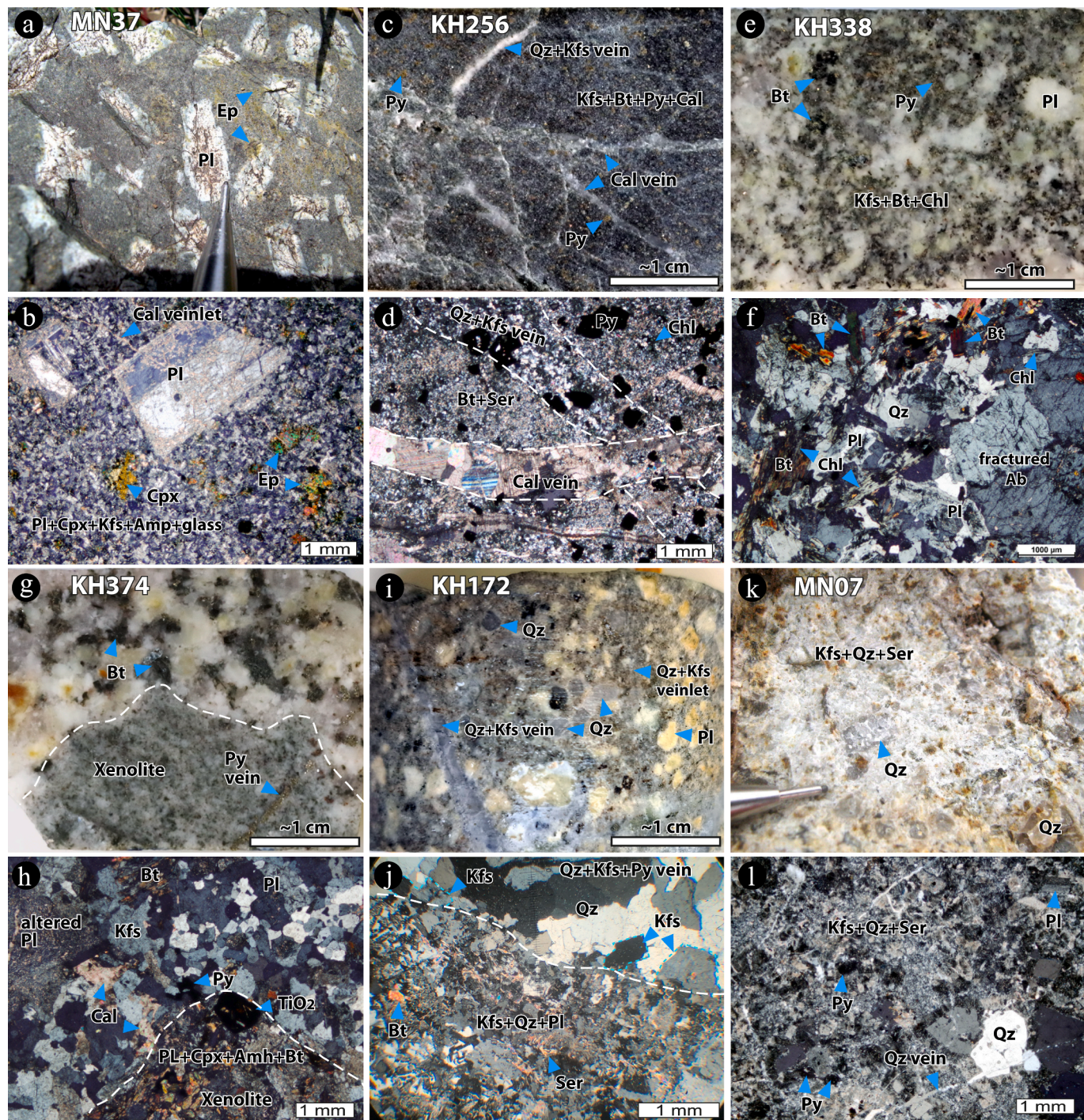


Fig. 2. Hand specimen and microscopic view (crossed polars) of the Eocene country rocks (a-d) and Oligocene-early Miocene subvolcanic rocks (e-l). (a) Porphyritic basaltic trachyandesite with patches and veinlets of Ep at the hand sample and (b) microscopic scale (sample MN37). (c) Qz + Kfs and Cal veining in andesitic tuff at the hand sample and microscopic scale KH256 (d), showing early Qz + Kfs and late Cal veins and disseminated Bt + Ser + Chl + Py. (e) Hand sample KH338 and (f) microscopic view of the early granodiorite porphyry, respectively, showing Chl replacement on Bt. (g-h) macroscopic and microscopic view of granite body (sample KH374), respectively, showing a granular texture and disseminated Py + Ser + Cal. (i-j) macroscopic and microscopic view of granite porphyry body (sample KH172), respectively, showing early Qz + Kfs veins and disseminated Ser selvage. (k-l) macroscopic and microscopic views of an early Miocene rhyodacite porphyry dyke (sample MN07), respectively, showing Qz phenocrysts in a matrix consisting of Qz + Kfs + Ser. Note the fracturing and narrow Qz veinlets in the microscopic image. Note: For mineral abbreviations see Table 1.

by Rabiee et al. (2019; Fig. 1 b). The lithology and alteration maps were prepared at the 1:5,000 scale, combining fieldwork with the available borehole stratigraphy (borehole KH02, drilled to a depth of 439 m; Fig. 1c-d), aiming at identifying the main magmatic bodies and associated alteration and mineralization zones/events (Fig. 1c). The classification of the magmatic rock types follows IUGS rules (Le Maitre et al.,

2005), and their petrographic description is provided in Table 1.

Ten samples were analysed for whole-rock chemistry via X-ray fluorescence (XRF) and inductively coupled plasma mass spectrometry (ICP-MS) methods to characterise their geochemical fingerprints. The whole-rock chemical composition of ten magmatic rock samples from KHD are presented in Table 2.

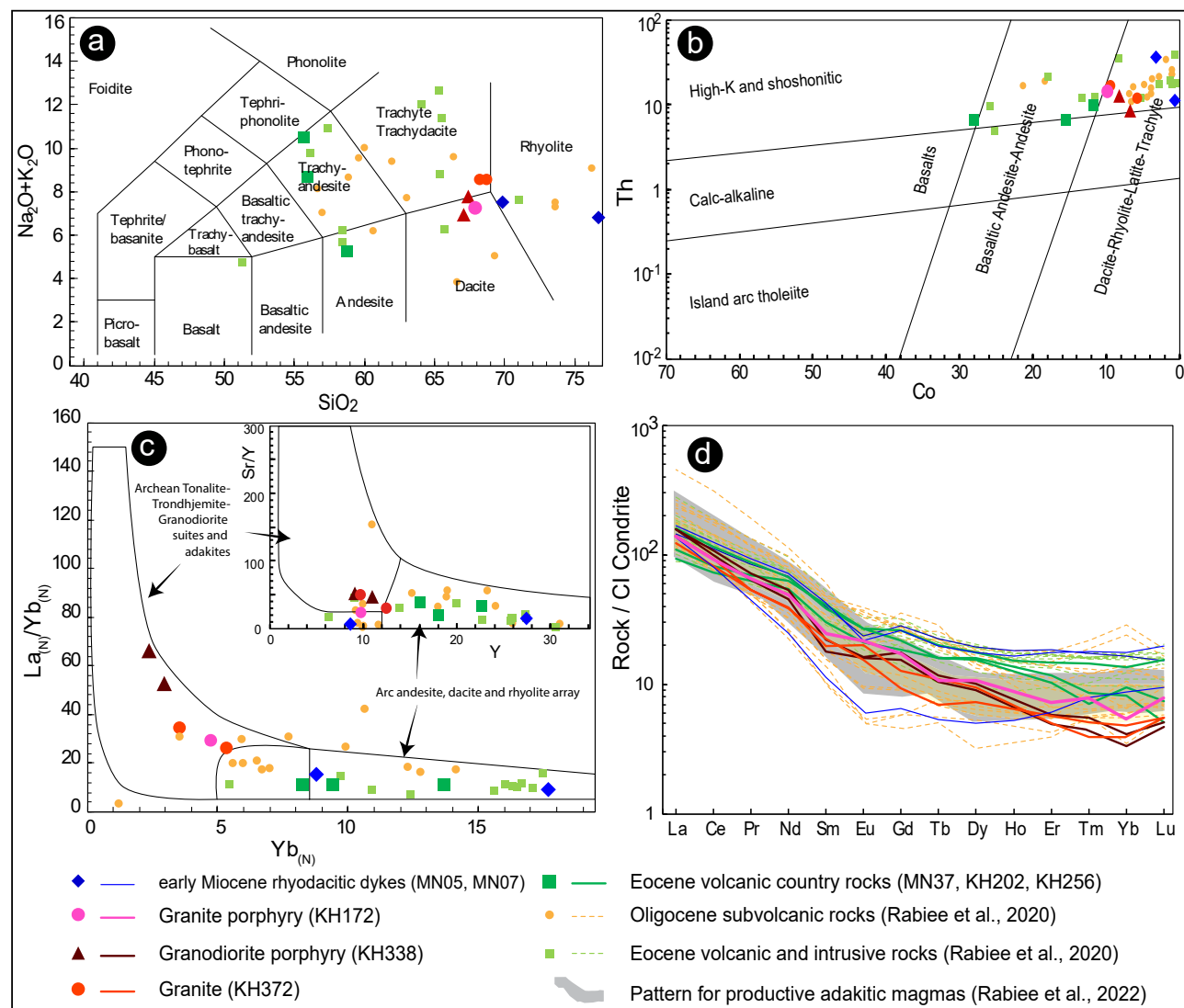


Fig. 3. (a) The total alkali–silica (TAS) chemical classification diagram (Le Maitre et al., 2005) for the Eocene–Miocene igneous rocks collected from the KHD (large symbols), and the Mianeh-Hashtroud magmatic zone (smaller symbols; data from Rabiee et al., 2020). (b) The same samples are plotted on the Th vs Co classification diagram for altered rocks (Hastie et al., 2007). (c) CI Chondrite-normalized (La/Yb)_N vs Yb _N discrimination diagram for adakites and calc-alkaline arc rocks (Martin, 1987) and Sr/Y vs Y diagram of Drummond and Defant (1990). (d) Chondrite-normalized (after Palme and O’Neill (2014)) REE patterns for the KHD samples compared to those of the Mianeh-Hashtroud (data from Rabiee et al., 2020) with the pattern of productive adakitic magmas along the UDMA presented by Rabiee et al. (2022) is shown as a grey polygon.

Six igneous rocks were selected for zircon U-Pb geochronology through the laser ablation inductively coupled plasma mass spectrometry (LA –ICP-MS), including two Eocene country rocks (MN37, KH256) and four subvolcanic rocks (MN07, KH-172, KH-338, KH-374). One molybdenite sample from the main ore zone (KH256) was selected for Re-Os dating. The analytical protocols are described in Supplementary Materials 1, representative CL-SEM imaging of the dated zircons is provided in Supplementary Materials 2, and results of the quality control of the LA-ICP-MS measurements for zircon standards are provided in Supplementary Materials 3. In the following, mineral abbreviations are after Whitney and Evans (2010).

4. Results

4.1. Geology and rock types

The Eocene country rocks of the KHD consist of porphyritic andesitic lava beds (sample MN37) and pyroclastic layers (samples KH202 and KH256; Table 1; Fig. 2a-d). These volcanic rocks are intruded by NE-

elongated granite porphyry stocks, characterised by feldspar and quartz phenocrysts and stockwork veining (sample KH172; Table 1 and Fig. 2i-j). A set of NE-striking barren rhyolite and rhyodacite dykes (samples MN05 and MN07; Table 1 and Fig. 2k-l) cut the granite porphyries and the altered volcanic host rocks, showing a fractured morphology and quartz micro veinlets (Fig. 1c-d). Additional granitoid porphyries are also found in the borehole (below 265 m; sample KH338, shallower, and sample KH374, deeper; Fig. 2e-h). Sample KH338 is a micro-porphyritic granodiorite, rich in plagioclase and biotite. Plagioclase grains are usually subhedral, partially resorbed and rimmed by secondary K-feldspar. The grains show an unusual fracturing with reddish to brownish biotite grains that are overprinted by secondary chlorite. Disseminated pyrite is present in about 3–5 % vol, usually associated with K-feldspar and quartz (Table 1 and Fig. 2e-f). Sample KH374 is a granular granite and contains 3–5 % vol of secondary pyrite associated with minor Mo mineralization. The sample shows evidence of propylitic alteration typified by chlorite + TiO_2 polymorphs overprinting magmatic biotite, and late sericite + carbonate overprinting plagioclase grains, (Table 1 and Fig. 2g-h). Microgranular biotite-rich

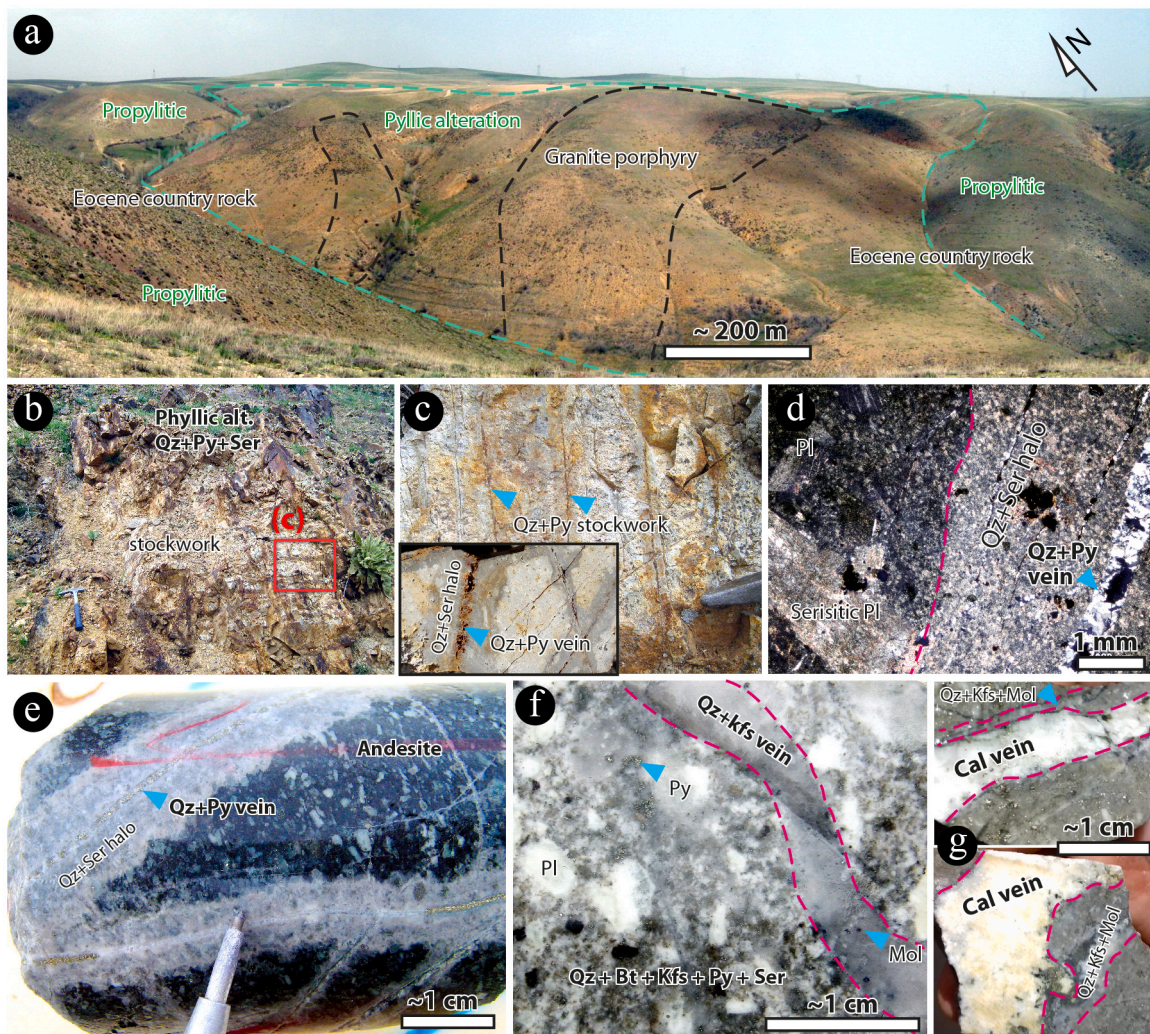


Fig. 4. (a) General field view of the KHD. The outcrops of the granitoid porphyry body are shown with dashed black line patterns whereas the green dashed lines show transitions from the different alteration zones. (b) Close-up of the phyllitic alteration with stockwork veining. (c) Closer view of the same stockwork veining in panel “b”. (d) Microscopic view of a type-D vein consisting of Qz + Py with a distinct sericitic halo (crossed polars). (e) Unoxidized type-D stockwork veins from unaltered levels of the borehole occurred in a porphyritic andesite. (f) Early Qz + Kfs vein with minor Mol mineralization in a matrix with disseminated Qz + Bt + Kfs + Py + Ser alteration assemblage in the Oligocene granite porphyry (sample KH172). (g) Two rock slabs with Cal veins showing rims consisting of Kfs + Qz + Mol mineralization in a strongly altered (with abundant Py) Eocene volcanic country rock. For mineral abbreviations see Table 1. (For interpretation of the references to colour in this figure legend, the reader is referred to the web version of this article.)

enclaves are present which contain early mineralised veins truncated from the enclave rims, and disseminated aggregates of pyrite, calcite, and TiO_2 polymorphs.

4.2. Whole rock chemical composition

In the total alkali vs silica (TAS) diagram (Le Maitre et al., 2005), the Eocene country rock samples show an andesitic to trachyandesitic composition, whereas the granitoid porphyries plot in the dacite field, and the dykes show a rhyolitic composition (Fig. 3a). In the classification diagrams based on immobile trace elements for hydrothermally altered rocks (Hastie et al., 2007), all samples show a high-K and shoshonitic signature, spanning from basaltic-andesite (country rocks) to dacite-rhyolite-trachyte (granitoid porphyries and dykes) compositions (Fig. 3b).

The chondrite-normalized Rare Earth Elements (REE) patterns show a pronounced enrichment in light REE (LREE) with distinct fractionation of middle (MREE) and heavy REE (HREE). Whereas the Eocene country rocks and the dyke samples show concave upward or flat MREE and HREE patterns, the granitoid bodies samples show a pronounced

depletion in HREE (Fig. 3d). Significantly, in the $(La/Yb)_N$ vs Y_{B_N} (Martin, 1987) and Sr/Y vs Y (Defant and Drummond, 1990) diagrams, the Eocene country rocks and the dykes fall within the field of volcanic arc magmatism whereas the granitoid bodies show an adakitic signature (Fig. 3c). The Sr/Y , $(La/Yb)_N$, $(Dy/Yb)_N$, and Eu/Eu^* ($Eu/Eu^* = Eu_N / (Sm_N \times Gd_N)^{0.5}$) values, where the subscript ‘N’ denotes chondrite-normalised values after Sun and McDonough (1989), range 20.7 – 38.7, 11.3 – 11.7, 1.2 – 1.8, and 0.85 – 0.90 for the Eocene country rocks and 24.8 – 52.4, 26.3 – 118.4, 1.3 – 8.6, and 0.82 – 1.26 for the granitoid bodies, respectively. These values for the dykes range 5.7 – 14.7, 9.4 – 15.6, 0.5 – 0.9, and 0.32 – 0.64, respectively (Table 2).

4.3. Alteration and veining

Alteration intensity increases toward the outcrops of the granitoid stocks as well as along the main gorge crossing these magmatic bodies, subparallel to a major NW-SE striking fault zone (Fig. 1c, 4a). Phyllitic alteration, with a whitish/yellowish appearance (Fig. 4b) forms the alteration core (~600 × 800 m wide area; Fig. 1c), both in veins and disseminated (see Sillitoe, 2010; Fig. 4a-e). A widespread propylitic

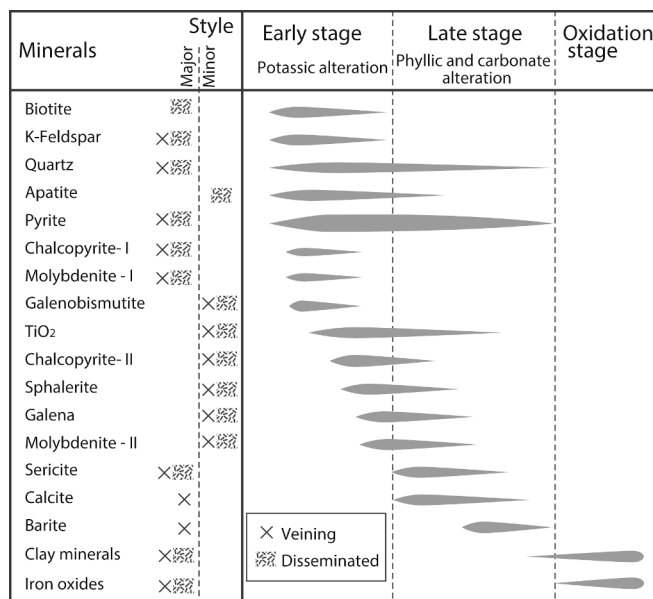


Fig. 5. The mineral assemblages associated with each alteration stage in the Khatoon-Abad prospect.

alteration zone envelops the phyllitic alteration (Fig. 2a, b, 4a), whose intensity rapidly decreases toward the marginal zones. While type-D quartz + pyrite veins ($\sim 0.5\text{--}3$ mm wide) with a sericitic halo (up to 1 cm wide) are common within the phyllitic alteration zone hosted in the volcanic country rocks (Fig. 4 a-e), less common quartz ± K-feldspar veins (< 5 mm wide) are present within the granitoid porphyry stock associated with minor molybdenite along the vein (Fig. 2i, j, 4f). Argillic and silicic alterations are locally observed within the altered zone, driven by structurally controlled fluid flow (Fig. 1c). The potassic alteration is mainly observed in the deep levels of the borehole (below 110 m depth) mainly developed in the Eocene country rocks (Fig. 2c-d), whereas it weakly occurs within the adjacent granitoid porphyries. However, potassic alteration is strongly overprinted by phyllitic alteration in the peripheral volcanic rocks with both disseminated and veining style (Fig. 1d, 2c-f), while it occurs mainly as overgrowth on primary (igneous) minerals and sparse quartz + K-feldspar veining (Fig. 2i, j and 4f). A late stage carbonatization, primarily assisted by veining, overprints the early alterations (Fig. 2c, d, h, 4 g). Carbonatization is very strong within the volcanic country rocks but within the porphyry stocks it occurs as disseminated infilling textures and micro-veinlets (Fig. 2h).

4.4. Ore mineralization

The Cu and Mo mineralization occurs mainly in the deep levels (170–268 m), with average values of 0.09 wt% and 154 ppm, respectively (Fig. 1d; Table S1), while in the shallower levels (0–170 m) shows some enrichment, with average values of 0.04 wt% and 45 ppm, respectively. However, the Mo concentration continues to the depth of 416 m as scattered zones with higher grades (up to 854 ppm). From 268 to 374 m depth, the average Mo concentration is 91 ppm, whereas Cu is less than 0.02 wt%.

The mineralization sequence inferred from the microscopic studies is presented in Fig. 5. Pyrite is the most common sulphide mineral, being observed in all rock and alteration types (3–10 vol%), mainly as disseminated (Fig. 2c-f) but also as vein filling (Fig. 2c-f and 6a-m). Two styles of molybdenite mineralization are distinguished from the shallow to the deep levels of the borehole, associated with (i) quartz + K-feldspar veins in the granite porphyry (Fig. 4f), and (ii) quartz + K-feldspar + TiO₂ polymorphs at the rims of the carbonate veins that occur within the

potassic-phyllitic alteration zone in the volcanic country rocks (Fig. 4g, 6a-d). Furthermore, molybdenite formed in two stages as (i) early stage (Mol-I) with chalcopyrite (Ccp-I) mineralization, occurring mostly as disseminated, and (ii) in veins (Mol-II), associated with quartz + K-feldspar veining, and along the rims and cracks of some individual pyrites in association with chalcopyrite (Ccp-II) and followed/overprinted by sphalerite + galena + TiO₂ polymorphs (Fig. 6a, d-g). Galenobismutite inclusions in pyrite within the potassic alteration zone (Fig. 6e, l) and late barite as discontinuous fracture fillings within the carbonate vein arrays (Fig. 6h-j) are also seldom observed.

4.5. Zircon u-pb geochronology

The zircon U-Pb geochronology was performed on six zircon separates, including two samples from the Eocene volcanic country rocks (MN37 and KH256), three samples from the granitoid rocks (KH172, KH338, and KH374), and one sample from the late dykes (MN07). The full results are reported in Table 3 and the calculated ages for all samples are presented in Fig. 7. The Th/U values consistently exceed 0.3, suggesting an igneous origin (Rubatto, 2002; Kirkland et al., 2015).

Samples KH256 (tuff) and MN37 (andesite) from the country rocks provided Concordia and intercept ages of 44.0 ± 1.0 and 36.98 ± 0.82 Ma, respectively (Fig. 7a, b). The sample KH256 also shows an intercept age at 59.2 ± 1.4 Ma (with individual $^{238}\text{U}/^{206}\text{Pb}$ ages from ~ 66 to ~ 49 Ma) for the zircon antecrysts (Miller et al., 2007). The inherited zircons generally show resorbed rims with heterogeneous internal textures (Supplementary Materials 2), compatible with renewed melting and corrosion (Corfu et al., 2003). The inherited zircons provide clusters of $^{238}\text{U}/^{206}\text{Pb}$ ages at $\sim 1754\text{--}1219$, $\sim 762\text{--}429$, $\sim 250\text{--}170$, and $\sim 91\text{--}88$ Ma, respectively (Table 3). The granitoid porphyry (KH338 granodiorite, and the KH374 and KH172 granite) samples show Concordia ages of 26.93 ± 0.30 , 26.01 ± 0.26 , and 25.74 ± 0.34 Ma, respectively (Fig. 7c-e). The rhyolite dyke sample (MN07) shows an intercept age at 21.53 ± 0.35 Ma.

4.6. Molybdenite Re-Os geochronology

A molybdenite sample was collected for Re-Os chronology from the main Cu-Mo mineralised zone within the potassic alteration zone (depth interval 170–268 m), where the highest Mo grades (154 ppm) are observed (Table 4). This sample contains 110.8 ppm Re and 31.0 ppb ^{187}Os and yielded a Re-Os age of 26.75 ± 0.14 Ma (uncertainty includes analytical + tracer + decay constant; Table 4).

5. Discussion

5.1. Geochronological framework

The zircon U-Pb geochronology of the KHD shows that magmatism has been active since at least Paleocene (zircon antecrysts) to early Miocene (Fig. 8a), documenting a case of prolonged and stationary magmatism (~ 45 Myr: $\sim 66\text{--}21$ Ma time lapse). Occurrence of Paleocene intrusive stocks to the west of the study area (Takab zone; Badr et al., 2013; Azizi et al., 2019) suggests that the Paleocene magmatism in the KHD likely emplaced at deeper crustal levels than those sampled by the borehole.

The U-Pb zircon age of the granodiorite porphyry body dated at 26.93 ± 0.30 Ma (sample KH38), combined with the nearly coincident Re-Os molybdenite age of 26.75 ± 0.14 Ma for its peripheral highest-grade Mo-Cu mineralization, indicates that this was the productive magma, associated with formation of the early-stage mineralized potassic core and its peripheral propylitic alteration zone (Fig. 8a-b).

5.2. Fertility and productivity of the different magma pulses

Here, we discuss the “fertility” and “productivity” of each magmatic

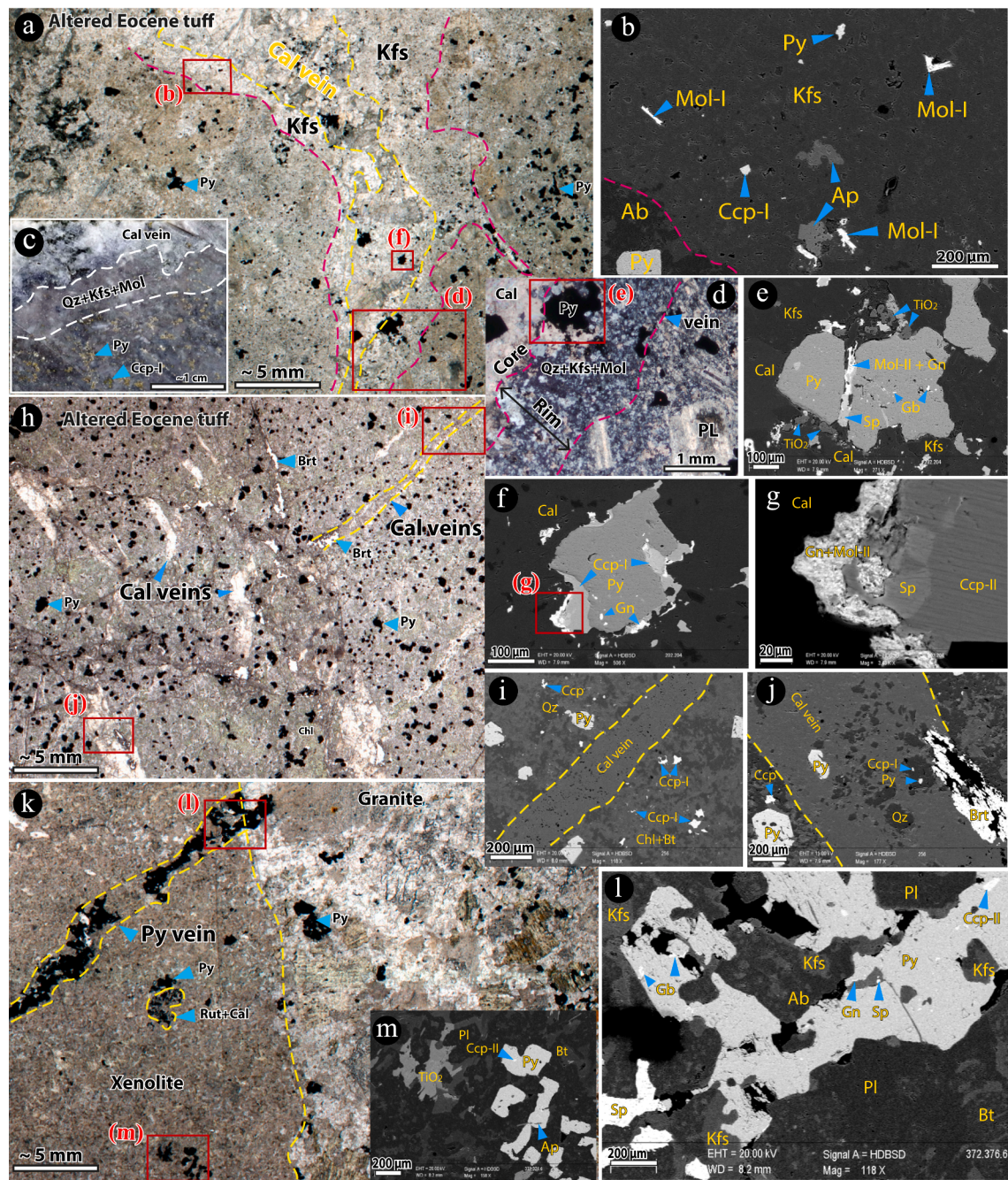


Fig. 6. Rock slabs (a, h, k; Samples KH202, KH256, KH374) showing the rock texture, veining and mineralization. (b) Backscattered electron (BSE) image from a Qz + Kfs + Mol mineralization in the rim of a Cal vein from panel “a” associated with Mol-I and Ccp-I. (c) close view of the rock slab along the complex Qz + Kfs + Cal vein rim, (d) microscopic image (crossed polars) from the rim of the same vein from panel “a”. (e-g) BSE images from Py grains in the vein and associated mineralization Mol-II and Ccp-II mineralization as inclusions, infilling cracks and Py rims. (i-j) BSE images from the Cal veins, some of which with minor Py and Brt, occurred in the potassic alteration with disseminated Ccp-I mineralization. (m-l) BSE images showing from a Py grains and vein associated with TiO₂ polymorphs, Ccp-II, Gb, Gn, Sp. Abbreviations: Py, Pyrite; Ccp, Chalcopyrite; Mol, Molybdenite; Sp, Sphalerite; Gn, Galena; Gb, Galnobismutite.

pulse within the context of the ore-bearing potential of the magma and the corresponding characteristics (size and ore grade) of the resulting mineralized ore bodies.

Prolonged stationary magmatism has been proposed as a key factor controlling the formation of porphyry deposits (Richards, 2000; Moritz et al., 2016; Rezeau et al., 2016; Rabiee et al., 2022), leading to generation of more water/metal/sulphur enriched magmas through continuous crystallization and fractionation processes (Loucks, 2014; Chiaradia and Caricchi, 2017; Richards et al., 2018; Lee and Tang, 2020). Indeed, the REE patterns of the Oligocene magmas overlap with

those of productive “adakitic” magmas along the UDMA (Rabiee et al., 2022). Significantly, unlike the Arasbaran metallogenic belt (Rabiee et al., 2022) of NW-Iran (Fig. 1a), the Early Miocene magmatism in the KHD does not show an adakite-like fingerprint and their REE patterns clearly indicate their unproductive signature (e.g., lower La_N/Yb_N values; Fig. 3c-d).

As discussed in the previous section, the main ore mineralisation is related to the emplacement of the early granodiorite porphyry body at ~ 27 Ma (sample KH38). The two younger Oligocene granitic bodies (dated at ~ 26.0 Ma and ~ 25.7 Ma, respectively) were emplaced ~ 1

Table 3

LA-ICP-MS U-(Th)-Pb zircon results for the magmatic samples in the KHD.

Sample name	Th/U	$^{207}\text{Pb}/^{206}\text{Pb}$	$^{207}\text{Pb}/^{235}\text{U}$	$^{206}\text{Pb}/^{238}\text{U}$	$^{208}\text{Pb}/^{232}\text{Th}$	ρ ($^{206}\text{Pb}/^{238}\text{U}$ vs. $^{207}\text{Pb}/^{235}\text{U}$)	$^{206}\text{Pb}/^{238}\text{U}$ age (Ma)	$^{207}\text{Pb}/^{235}\text{U}$ age (Ma)	$^{208}\text{Pb}/^{232}\text{Th}$ age (Ma)
KH256; Andesitic tuff; 44 ± 1 Ma (antecrysts: 59.2 ± 1.4 Ma)									
KH256-1	2.28 ± 0.23	0.062 ± 0.012	0.059 ± 0.011	0.00753 ± 0.00086	–	0.45	48.3 ± 5.5	60 ± 12	–
KH256-1b	2.87 ± 0.24	0.047 ± 0.021	0.105 ± 0.022	0.00716 ± 0.00069	0.00544 ± 0.00074	0.26	46.0 ± 4.4	42 ± 20	110 ± 15
KH256-1c	2.20 ± 0.16	0.047 ± 0.016	0.064 ± 0.013	0.00742 ± 0.00061	0.00347 ± 0.00054	–0.07	47.6 ± 3.9	37 ± 12	70 ± 11
KH256-2	0.836 ± 0.071	0.0550 ± 0.0081	0.068 ± 0.011	0.0093 ± 0.0010	–	0.56	59.5 ± 6.7	66 ± 11	–
KH256-3	1.28 ± 0.11	0.058 ± 0.012	0.079 ± 0.016	0.00958 ± 0.00090	–	0.45	61.4 ± 5.7	76 ± 15	–
KH256-4	1.79 ± 0.11	0.0418 ± 0.0095	0.0370 ± 0.0081	0.00659 ± 0.00056	–	0.24	42.3 ± 3.6	36.4 ± 7.9	–
KH256-4b	0.908 ± 0.071	0.0469 ± 0.0067	0.0436 ± 0.0046	0.00697 ± 0.00048	0.00204 ± 0.00014	–0.05	44.7 ± 3.1	38.4 ± 4.6	41.1 ± 2.8
KH256-4c	0.919 ± 0.064	0.0470 ± 0.0078	0.0567 ± 0.0094	0.00722 ± 0.00048	0.00239 ± 0.00018	0.01	46.4 ± 3.0	44.4 ± 9.0	48.2 ± 3.7
KH256-6	0.873 ± 0.059	0.097 ± 0.046	0.095 ± 0.040	0.0093 ± 0.0013	–	–0.14	59.8 ± 8.4	84 ± 36	–
KH256-7	1.56 ± 0.14	0.057 ± 0.018	0.065 ± 0.019	0.0096 ± 0.0011	–	0.09	61.8 ± 7.1	62 ± 18	–
KH256-8	1.93 ± 0.13	0.046 ± 0.020	0.057 ± 0.024	0.00913 ± 0.00093	–	0.23	58.5 ± 5.9	53 ± 22	–
KH256-9	2.38 ± 0.15	0.0536 ± 0.0094	0.065 ± 0.011	0.00921 ± 0.00079	–	0.29	59.0 ± 5.0	63 ± 11	–
KH256-10a	1.49 ± 0.15	0.048 ± 0.024	0.040 ± 0.019	0.00684 ± 0.00078	–	–0.14	43.9 ± 5.0	39 ± 18	–
KH256-10B	2.23 ± 0.23	0.059 ± 0.013	0.135 ± 0.029	0.0182 ± 0.0025	–	0.31	116 ± 16	127 ± 26	–
KH256-10b	1.24 ± 0.10	0.047 ± 0.016	0.054 ± 0.016	0.00735 ± 0.00059	0.00315 ± 0.00039	0.00	47.2 ± 3.8	42 ± 16	63.6 ± 7.9
KH256-10c	1.033 ± 0.076	0.047 ± 0.017	0.055 ± 0.014	0.00687 ± 0.00049	0.00203 ± 0.00022	–0.10	44.1 ± 3.2	47 ± 13	40.9 ± 4.5
KH256-11	1.238 ± 0.072	0.046 ± 0.016	0.061 ± 0.020	0.00935 ± 0.00079	–	0.24	59.9 ± 5.0	58 ± 18	–
KH256-12	2.39 ± 0.22	0.059 ± 0.022	0.067 ± 0.021	0.00896 ± 0.00087	–	0.28	57.4 ± 5.6	67 ± 21	–
KH256-13	1.53 ± 0.10	0.043 ± 0.020	0.059 ± 0.027	0.0099 ± 0.0012	–	0.22	63.3 ± 7.6	54 ± 25	–
KH256-14	1.137 ± 0.077	0.060 ± 0.016	0.071 ± 0.018	0.00942 ± 0.00077	–	0.30	60.4 ± 4.9	68 ± 17	–
KH256-15	2.07 ± 0.17	0.043 ± 0.024	0.062 ± 0.034	0.0100 ± 0.0014	–	0.00	64.3 ± 8.8	62 ± 33	–
KH256-16	1.133 ± 0.085	0.129 ± 0.052	0.153 ± 0.067	0.0104 ± 0.0017	–	–0.16	66 ± 11	130 ± 53	–
KH256-17	2.05 ± 0.12	0.069 ± 0.070	0.024 ± 0.034	0.0069 ± 0.0012	–	0.09	44.2 ± 7.5	24 ± 36	–
KH256-18	0.751 ± 0.040	0.048 ± 0.052	0.21 ± 0.14	0.0102 ± 0.0017	–	0.17	65 ± 11	108 ± 87	–
KH256-19	1.169 ± 0.070	0.047 ± 0.019	0.052 ± 0.023	0.00869 ± 0.00087	–	0.20	55.8 ± 5.6	54 ± 24	–
KH256-20c	3.21 ± 0.25	0.066 ± 0.071	0.038 ± 0.054	0.0092 ± 0.0013	–	0.22	58.7 ± 8.4	23 ± 50	–
KH256-21	2.10 ± 0.16	0.036 ± 0.033	0.080 ± 0.051	0.0105 ± 0.0015	–	0.09	67.5 ± 9.3	66 ± 43	–
KH256-22c	2.68 ± 0.18	0.090 ± 0.074	0.11 ± 0.10	0.0098 ± 0.0015	–	0.42	62.7 ± 9.4	200 ± 170	–
KH256-23	1.53 ± 0.11	0.044 ± 0.016	0.052 ± 0.016	0.00899 ± 0.00086	–	–0.17	57.7 ± 5.5	50 ± 15	–
KH256-24	1.159 ± 0.067	0.049 ± 0.027	0.045 ± 0.022	0.00580 ± 0.00063	–	–0.05	37.3 ± 4.0	42 ± 21	–
KH256-24b	0.723 ± 0.057	0.134 ± 0.033	0.116 ± 0.028	0.00613 ± 0.00057	0.00297 ± 0.00041	0.12	39.4 ± 3.6	23 ± 28	60.0 ± 8.2
KH256-29	0.775 ± 0.084	0.047 ± 0.012	0.043 ± 0.011	0.00675 ± 0.00052	0.00237 ± 0.00018	–0.04	43.3 ± 3.3	43 ± 10	47.8 ± 3.7
MN37; Basaltic trachy-andesite; 36.98 ± 0.82 Ma									
MN37-01	0.60	0.0592 ± 0.0138	0.0489 ± 0.0117	0.006 ± 0.0003	0.0023 ± 0.0003	0.23	38.54 ± 2.1	48.52 ± 11.63	46.41 ± 11.85
MN37-02	0.80	0.062 ± 0.0196	0.0706 ± 0.0229	0.0083 ± 0.0006	0.0025 ± 0.0004	0.22	53 ± 3.81	69.24 ± 22.48	50.44 ± 15.8
MN37-03	0.77	0.0599 ± 0.0125	0.0615 ± 0.0132	0.0074 ± 0.0004	0.0026 ± 0.0003	0.23	46.11 ± 2.31	30.77 ± 6.63	52.46 ± 11.85
MN37-04	0.66	0.0519 ± 0.0083	0.0417 ± 0.0068	0.0058 ± 0.0002	0.0021 ± 0.0002	0.23	36.33 ± 1.36	21.42 ± 3.52	42.38 ± 7.9
MN37-05	1.02	0.048 ± 0.0057	0.0375 ± 0.0046	0.0057 ± 0.0002	0.002 ± 0.0001	0.24	36.42 ± 1.05	37.34 ± 4.55	40.36 ± 3.95
MN37-06	1.40	0.1177 ± 0.0146	0.1036 ± 0.0135	0.0064 ± 0.0003	0.0038 ± 0.0002	0.32	34.2 ± 1.44	–19.51 ± –2.55	76.62 ± 7.89
MN37-07	1.49	0.0724 ± 0.0119	0.0636 ± 0.0108	0.0064 ± 0.0003	0.0023 ± 0.0001	0.26	39.68 ± 1.75	40.81 ± 6.94	46.41 ± 3.95
MN37-08	0.99	0.0554 ± 0.0108	0.0524 ± 0.0105	0.0069 ± 0.0003	0.0022 ± 0.0002	0.23	42.59 ± 1.94	26.25 ± 5.27	44.4 ± 7.9
MN37-09	0.88	0.0528 ± 0.0063	0.2841 ± 0.0348	0.0391 ± 0.0012	0.0134 ± 0.0007	0.24	233.21 ± 6.95	29.39 ± 3.6	268.91 ± 27.35
MN37-11	1.29	0.0477 ± 0.0094	0.0343 ± 0.0069	0.0052 ± 0.0002	0.0018 ± 0.0001	0.22	33.54 ± 1.48	34.22 ± 6.9	36.33 ± 3.95
MN37-12	0.83	0.0755 ± 0.0045	1.3391 ± 0.0839	0.1286 ± 0.0026	0.0423 ± 0.0013	0.33	762.27 ± 15.63	696.21 ± 43.63	836.97 ± 49.38
MN37-13	0.82	0.0495 ± 0.0069	0.0603 ± 0.0086	0.0088 ± 0.0003	0.0029 ± 0.0002	0.23	56.15 ± 1.85	51.11 ± 7.31	58.5 ± 7.9
MN37-14	0.65	0.0921 ± 0.0044	0.5322 ± 0.0271	0.0419 ± 0.0008	0.0221 ± 0.0005	0.37	250.24 ± 4.72	236.81 ± 12.08	441.6 ± 19.37
MN37-15	0.54	0.0571 ± 0.0035	0.5473 ± 0.0352	0.0695 ± 0.0014	0.0238 ± 0.0008	0.30	428.82 ± 8.34	388.34 ± 24.98	475.18 ± 30.94
MN37-16	0.30	0.0499 ± 0.003	0.0951 ± 0.0061	0.0138 ± 0.0003	0.0049 ± 0.0002	0.29	88.02 ± 1.65	84.78 ± 5.41	98.75 ± 7.88
MN37-17	0.44	0.0609 ± 0.0036	0.9264 ± 0.0579	0.1104 ± 0.002	0.0354 ± 0.0015	0.29	672.49 ± 12.1	638.48 ± 39.91	702.78 ± 57.36
MN37-18	0.60	0.0954 ± 0.0026	3.6199 ± 0.1117	0.2752 ± 0.0037	0.0887 ± 0.0022	0.44	1567.08 ± 21.17	1553.85 ± 47.93	1716.86 ± 80.01
MN37-19	0.57	0.1153 ± 0.0031	4.9784 ± 0.1497	0.3131 ± 0.0043	0.0979 ± 0.0026	0.46	1754.28 ± 24.13	1809.78 ± 54.42	1886.85 ± 93.77
MN37-20	0.15	0.0777 ± 0.0029	2.2298 ± 0.0885	0.2082 ± 0.0031	0.0744 ± 0.0035	0.37	1219.21 ± 17.88	1190.42 ± 47.26	1449.74 ± 128.99

(continued on next page)

Table 3 (continued)

Sample name	Th/U	$^{207}\text{Pb}/^{206}\text{Pb}$	$^{207}\text{Pb}/^{235}\text{U}$	$^{206}\text{Pb}/^{238}\text{U}$	$^{208}\text{Pb}/^{232}\text{Th}$	ρ ($^{206}\text{Pb}/^{238}\text{U}$ vs. $^{207}\text{Pb}/^{235}\text{U}$)	$^{206}\text{Pb}/^{238}\text{U}$ age (Ma)	$^{207}\text{Pb}/^{235}\text{U}$ age (Ma)	$^{208}\text{Pb}/^{232}\text{Th}$ age (Ma)
MN37-21	0.52	0.0354 ± 0.0184	0.0409 ± 0.0215	0.0084 ± 0.0007	0.0061 ± 0.0009	0.16	53.66 ± 4.57	40.65 ± 21.39	122.86 ± 35.42
MN37-23	0.82	0.1431 ± 0.0165	0.1124 ± 0.0138	0.0057 ± 0.0002	0.0037 ± 0.0002	0.34	34.51 ± 1.45	72.8 ± 8.95	74.61 ± 7.89
MN37-24	0.78	0.1224 ± 0.0141	0.1433 ± 0.0175	0.0085 ± 0.0003	0.0062 ± 0.0003	0.32	50.98 ± 2.01	77.72 ± 9.47	124.87 ± 11.81
MN37-25	0.83	0.0478 ± 0.011	0.0505 ± 0.0119	0.0077 ± 0.0004	0.0026 ± 0.0002	0.21	49.18 ± 2.42	50.02 ± 11.75	52.46 ± 7.9
MN37-26	1.63	0.0895 ± 0.0157	0.0763 ± 0.014	0.0062 ± 0.0003	0.0024 ± 0.0002	0.28	33.13 ± 1.7	-44.5 ± -8.14	48.43 ± 7.9
MN37-27	0.15	0.0495 ± 0.004	0.1823 ± 0.0153	0.0267 ± 0.0006	0.0094 ± 0.0008	0.28	169.8 ± 3.94	166.45 ± 13.92	189.01 ± 31.38
MN37-28	0.96	0.0643 ± 0.0033	1.0022 ± 0.0549	0.113 ± 0.0022	0.0409 ± 0.0012	0.36	689.4 ± 13.64	699.38 ± 38.3	809.81 ± 45.65
MN37-29	0.40	0.0538 ± 0.0053	0.2691 ± 0.0276	0.0363 ± 0.001	0.0142 ± 0.0009	0.26	229.56 ± 6.2	242 ± 24.83	284.85 ± 35.14
MN37-30	0.68	0.049 ± 0.0035	0.2259 ± 0.0167	0.0334 ± 0.0007	0.0115 ± 0.0004	0.29	212.08 ± 4.59	206.8 ± 15.26	231 ± 15.66
MN37-31	0.98	0.0441 ± 0.0162	0.0368 ± 0.0138	0.0061 ± 0.0004	0.002 ± 0.0003	0.19	38.93 ± 2.7	36.68 ± 13.74	40.36 ± 11.85
MN37-32	0.45	0.2918 ± 0.0203	0.8699 ± 0.068	0.0216 ± 0.0008	0.0342 ± 0.0015	0.46	91.42 ± 3.27	23.88 ± 1.87	679.36 ± 57.43
KH338; Granodiorite porphyry; 26.93 ± 0.30 Ma									
KH338-1	1.418 ± 0.066	0.0454 ± 0.0087	0.0225 ± 0.0045	0.00411 ± 0.00023	0.00136 ± 0.00013	-0.11	26.4 ± 1.5	22.4 ± 4.5	27.6 ± 2.7
KH338-2	1.953 ± 0.090	0.039 ± 0.014	0.0208 ± 0.0073	0.00453 ± 0.00028	0.00152 ± 0.00032	0.16	29.1 ± 1.8	20.5 ± 7.3	30.6 ± 6.5
KH338-3	0.792 ± 0.038	0.0436 ± 0.0079	0.0204 ± 0.0035	0.00421 ± 0.00023	0.001398 ± 0.000082	-0.07	27.1 ± 1.5	20.4 ± 3.5	28.2 ± 1.7
KH338-4	0.895 ± 0.037	0.0484 ± 0.0095	0.0230 ± 0.0044	0.00427 ± 0.00027	0.00141 ± 0.00011	0.15	27.5 ± 1.8	23.0 ± 4.3	28.5 ± 2.2
KH338-5	1.959 ± 0.088	0.054 ± 0.013	0.0282 ± 0.0075	0.00404 ± 0.00037	0.00135 ± 0.00019	0.32	26.0 ± 2.4	27.8 ± 7.3	27.4 ± 3.8
KH338-6	0.434 ± 0.018	0.0400 ± 0.0036	0.0204 ± 0.0018	0.00427 ± 0.00019	0.001364 ± 0.000064	0.31	27.5 ± 1.2	20.4 ± 1.8	27.6 ± 1.3
KH338-7	0.904 ± 0.058	0.061 ± 0.033	0.028 ± 0.014	0.00388 ± 0.00071	0.00146 ± 0.00026	0.02	24.9 ± 4.6	27 ± 14	29.4 ± 5.2
KH338-8	1.19 ± 0.12	0.045 ± 0.013	0.0223 ± 0.0065	0.00455 ± 0.00028	0.00151 ± 0.00017	0.03	29.3 ± 1.8	22.2 ± 6.4	30.5 ± 3.3
KH338-9	1.304 ± 0.071	0.041 ± 0.012	0.0250 ± 0.0091	0.00463 ± 0.00031	0.00153 ± 0.00018	0.36	29.8 ± 2.0	24.5 ± 8.7	30.9 ± 3.7
KH338-10	1.64 ± 0.12	0.043 ± 0.012	0.0208 ± 0.0062	0.00439 ± 0.00032	0.00137 ± 0.00026	0.12	28.2 ± 2.1	20.7 ± 6.2	27.7 ± 5.2
KH338-11	1.902 ± 0.081	0.047 ± 0.014	0.0221 ± 0.0071	0.00410 ± 0.00023	0.00115 ± 0.00019	-0.36	26.3 ± 1.5	21.8 ± 7.0	23.2 ± 3.8
KH338-12	2.36 ± 0.21	0.0451 ± 0.0081	0.0215 ± 0.0035	0.00431 ± 0.00018	0.00141 ± 0.00017	0.16	27.7 ± 1.2	21.6 ± 3.5	28.4 ± 3.5
KH338-13	1.91 ± 0.15	0.061 ± 0.018	0.037 ± 0.011	0.00417 ± 0.00041	-	0.36	26.8 ± 2.6	36 ± 11	-
KH338-14	0.844 ± 0.070	0.069 ± 0.010	0.0409 ± 0.0076	0.00411 ± 0.00040	-	0.53	26.4 ± 2.6	40.5 ± 7.4	-
KH338-15	1.89 ± 0.16	0.053 ± 0.010	0.0327 ± 0.0068	0.00478 ± 0.00044	-	0.40	30.7 ± 2.8	32.5 ± 6.7	-
KH338-16	2.12 ± 0.14	0.049 ± 0.013	0.0265 ± 0.0072	0.00425 ± 0.00038	-	0.08	27.3 ± 2.4	26.3 ± 7.1	-
KH338-17	1.47 ± 0.14	0.066 ± 0.011	0.0372 ± 0.0063	0.00433 ± 0.00030	-	0.11	27.9 ± 1.9	36.8 ± 6.1	-
KH338-18	3.21 ± 0.17	0.0587 ± 0.0093	0.0369 ± 0.0059	0.00455 ± 0.00030	-	0.11	29.3 ± 1.9	36.6 ± 5.7	-
KH338-19	1.68 ± 0.14	0.065 ± 0.014	0.0393 ± 0.0081	0.00447 ± 0.00047	-	0.04	28.8 ± 3.0	38.7 ± 7.9	-
KH338-20	3.24 ± 0.27	0.0597 ± 0.0095	0.0359 ± 0.0059	0.00463 ± 0.00041	-	0.11	29.8 ± 2.6	35.6 ± 5.7	-
KH338-21	1.250 ± 0.089	0.052 ± 0.017	0.0297 ± 0.0098	0.00412 ± 0.00038	-	0.20	26.5 ± 2.4	29.0 ± 9.6	-
KH338-22	1.52 ± 0.12	0.048 ± 0.012	0.0262 ± 0.0063	0.00459 ± 0.00035	-	-0.02	29.5 ± 2.2	27.4 ± 6.8	-
KH338-23a	2.11 ± 0.27	0.046 ± 0.022	0.026 ± 0.011	0.00498 ± 0.00071	-	0.10	32.0 ± 4.5	26 ± 10	-
KH338-23b	1.36 ± 0.13	0.0464 ± 0.0077	0.0270 ± 0.0048	0.00432 ± 0.00036	-	0.35	27.8 ± 2.3	27.0 ± 4.7	-
KH338-24	2.62 ± 0.18	0.046 ± 0.016	0.0288 ± 0.0090	0.00452 ± 0.00040	-	0.28	29.0 ± 2.6	28.2 ± 8.9	-
KH374; Granite; 26.01 ± 0.26 Ma									
KH374-1	2.007 ± 0.094	0.074 ± 0.013	0.0395 ± 0.0068	0.00432 ± 0.00018	0.00203 ± 0.00018	0.05	27.8 ± 1.1	39.1 ± 6.6	40.9 ± 3.7
KH374-2	1.440 ± 0.075	0.0465 ± 0.0088	0.0228 ± 0.0040	0.00400 ± 0.00019	0.00126 ± 0.00012	-0.29	25.8 ± 1.2	22.8 ± 4.0	25.4 ± 2.4
KH374-3	2.04 ± 0.11	0.083 ± 0.018	0.045 ± 0.010	0.00421 ± 0.00027	0.00251 ± 0.00024	-0.07	27.1 ± 1.8	44 ± 10	50.6 ± 4.8
KH374-4	1.729 ± 0.059	0.056 ± 0.011	0.0288 ± 0.0057	0.00413 ± 0.00020	0.00135 ± 0.00013	-0.01	26.6 ± 1.3	28.7 ± 5.6	27.3 ± 2.7
KH374-5	1.519 ± 0.090	0.052 ± 0.011	0.0292 ± 0.0064	0.00422 ± 0.00023	0.00126 ± 0.00020	0.06	27.1 ± 1.5	29.1 ± 6.3	25.5 ± 3.9
KH374-6c	1.841 ± 0.094	0.043 ± 0.011	0.0254 ± 0.0068	0.00449 ± 0.00024	0.00151 ± 0.00019	0.08	28.8 ± 1.6	25.2 ± 6.7	30.6 ± 3.8
KH374-8	1.257 ± 0.068	0.0434 ± 0.0084	0.0473 ± 0.0094	0.00887 ± 0.00038	0.00278 ± 0.00022	0.11	56.9 ± 2.4	46.5 ± 9.1	56.2 ± 4.5
KH374-9	1.988 ± 0.061	0.0503 ± 0.0076	0.0249 ± 0.0042	0.00381 ± 0.00023	0.00125 ± 0.00014	0.10	24.5 ± 1.5	24.9 ± 4.2	25.2 ± 2.8
KH374-10	1.048 ± 0.029	0.0463 ± 0.0075	0.0229 ± 0.0037	0.00412 ± 0.00014	0.001243 ± 0.000082	-0.01	26.48 ± 0.92	22.9 ± 3.7	25.1 ± 1.7
KH374-11c	0.538 ± 0.014	0.0496 ± 0.0072	0.0250 ± 0.0035	0.00415 ± 0.00015	0.001360 ± 0.000069	-0.06	26.69 ± 0.96	25.0 ± 3.4	27.5 ± 1.4
KH374-12	1.744 ± 0.058	0.0452 ± 0.0091	0.0219 ± 0.0042	0.00422 ± 0.00023	0.00125 ± 0.00018	0.08	27.1 ± 1.5	21.9 ± 4.1	25.3 ± 3.5
KH374-13	1.559 ± 0.074	0.0447 ± 0.0077	0.0256 ± 0.0043	0.00430 ± 0.00023	0.00133 ± 0.00010	-0.03	27.7 ± 1.5	25.5 ± 4.2	26.8 ± 2.1
KH374-14	1.300 ± 0.042	0.0492 ± 0.0087	0.0277 ± 0.0047	0.00419 ± 0.00016	0.00122 ± 0.00012	-0.08	26.9 ± 1.0	27.7 ± 4.7	24.7 ± 2.4
KH374-15	1.571 ± 0.039	0.0408 ± 0.0085	0.0210 ± 0.0042	0.00397 ± 0.00014	0.00133 ± 0.00014	0.01	25.52 ± 0.92	21.0 ± 4.2	26.9 ± 2.8
KH374-16A	1.330 ± 0.081	0.047 ± 0.011	0.0285 ± 0.0064	0.00443 ± 0.00033	0.00131 ± 0.00013	-0.06	28.5 ± 2.1	28.4 ± 6.3	26.5 ± 2.6

(continued on next page)

Table 3 (continued)

Sample name	Th/U	$^{207}\text{Pb}/^{206}\text{Pb}$	$^{207}\text{Pb}/^{235}\text{U}$	$^{206}\text{Pb}/^{238}\text{U}$	$^{208}\text{Pb}/^{232}\text{Th}$	ρ ($^{206}\text{Pb}/^{238}\text{U}$ vs. $^{207}\text{Pb}/^{235}\text{U}$)	$^{206}\text{Pb}/^{238}\text{U}$ age (Ma)	$^{207}\text{Pb}/^{235}\text{U}$ age (Ma)	$^{208}\text{Pb}/^{232}\text{Th}$ age (Ma)
KH374-16B	1.381 ± 0.073	0.045 ± 0.012	0.0261 ± 0.0076	0.00414 ± 0.00018	0.00118 ± 0.00017	0.30	26.6 ± 1.1	26.0 ± 7.5	23.8 ± 3.4
KH374-17	1.535 ± 0.037	0.0425 ± 0.0088	0.0234 ± 0.0049	0.00409 ± 0.00016	0.00121 ± 0.00012	-0.08	26.3 ± 1.0	23.4 ± 4.9	24.5 ± 2.4
KH374-18	2.24 ± 0.13	0.229 ± 0.060	0.199 ± 0.081	0.0060 ± 0.0011	0.0088 ± 0.0035	0.04	38.7 ± 7.2	168 ± 59	177 ± 70
KH374-19	1.866 ± 0.090	0.048 ± 0.010	0.0276 ± 0.0059	0.00414 ± 0.00017	0.00144 ± 0.00017	0.31	26.6 ± 1.1	27.5 ± 5.8	29.1 ± 3.5
KH374-20	1.466 ± 0.068	0.0476 ± 0.0072	0.0264 ± 0.0038	0.00402 ± 0.00018	0.00134 ± 0.00011	-0.24	25.9 ± 1.2	26.4 ± 3.8	27.1 ± 2.3
KH374-21	1.600 ± 0.070	0.076 ± 0.017	0.0400 ± 0.0086	0.00414 ± 0.00023	0.00164 ± 0.00017	0.33	26.6 ± 1.5	39.4 ± 8.3	33.0 ± 3.4
KH374-22	1.208 ± 0.072	0.0387 ± 0.0087	0.0218 ± 0.0050	0.00393 ± 0.00017	0.00123 ± 0.00011	-0.15	25.3 ± 1.1	21.7 ± 4.9	24.8 ± 2.3
KH374-23c	0.519 ± 0.016	0.0479 ± 0.0049	0.0278 ± 0.0027	0.00424 ± 0.00011	0.00149 ± 0.000061	-0.14	27.24 ± 0.71	27.8 ± 2.7	28.7 ± 1.2
KH374-24	0.948 ± 0.073	0.056 ± 0.016	0.0304 ± 0.0085	0.00411 ± 0.00027	0.00128 ± 0.00016	-0.34	26.4 ± 1.8	30.0 ± 8.3	25.9 ± 3.1
KH172; Granite porphyry; 25.74 ± 0.34 Ma									
KH172-1	0.882 ± 0.045	0.061 ± 0.012	0.0309 ± 0.0064	0.00398 ± 0.00031	0.00129 ± 0.00013	0.01	25.6 ± 2.0	30.6 ± 6.2	26.0 ± 2.5
KH172-2	1.529 ± 0.082	0.060 ± 0.011	0.0337 ± 0.0066	0.00437 ± 0.00034	0.00117 ± 0.00015	0.23	28.1 ± 2.2	34.6 ± 6.9	23.7 ± 3.1
KH172-3	1.397 ± 0.069	0.0471 ± 0.0089	0.0227 ± 0.0042	0.00401 ± 0.00028	0.00130 ± 0.00012	0.10	25.8 ± 1.8	22.6 ± 4.2	26.2 ± 2.4
KH172-4c	1.535 ± 0.087	0.0449 ± 0.0093	0.0229 ± 0.0051	0.00433 ± 0.00032	0.00142 ± 0.00012	0.11	27.9 ± 2.0	22.8 ± 5.0	28.8 ± 2.5
KH172-5c	1.795 ± 0.091	0.054 ± 0.024	0.0222 ± 0.011	0.00451 ± 0.00044	0.00120 ± 0.00030	0.22	29.0 ± 2.9	22 ± 11	24.3 ± 6.1
KH172-6c	1.33 ± 0.11	0.039 ± 0.010	0.0216 ± 0.0058	0.00413 ± 0.00023	0.00138 ± 0.00016	0.03	26.6 ± 1.5	21.4 ± 5.7	27.9 ± 3.2
KH172-7c	1.192 ± 0.068	0.055 ± 0.043	0.019 ± 0.015	0.00403 ± 0.00056	0.00129 ± 0.00032	0.00	25.9 ± 3.6	18 ± 14	26.0 ± 6.4
KH172-8	2.41 ± 0.12	0.053 ± 0.016	0.0266 ± 0.0077	0.00434 ± 0.00030	0.00143 ± 0.00025	0.12	27.9 ± 1.9	26.3 ± 7.5	28.8 ± 5.0
KH172-9	1.362 ± 0.093	0.0582 ± 0.0088	0.0317 ± 0.0052	0.00434 ± 0.00029	0.00147 ± 0.00012	0.09	27.9 ± 1.9	31.4 ± 5.1	29.6 ± 2.4
KH172-10	1.747 ± 0.096	0.0472 ± 0.0095	0.0249 ± 0.0050	0.00397 ± 0.00028	0.00135 ± 0.00014	0.16	25.5 ± 1.8	24.7 ± 4.9	27.3 ± 2.9
KH172-11	1.335 ± 0.074	0.0463 ± 0.0070	0.0230 ± 0.0037	0.00416 ± 0.00026	0.001196 ± 0.000091	0.10	26.8 ± 1.7	23.0 ± 3.7	24.2 ± 1.8
KH172-12	1.857 ± 0.096	0.0557 ± 0.0073	0.0265 ± 0.0036	0.00376 ± 0.00023	0.00122 ± 0.00011	0.23	24.2 ± 1.5	26.5 ± 3.5	24.6 ± 2.2
KH172-13	0.935 ± 0.032	0.0587 ± 0.0099	0.0309 ± 0.0047	0.00407 ± 0.00020	0.001362 ± 0.000090	-0.20	26.2 ± 1.3	30.7 ± 4.6	27.5 ± 1.8
KH172-14	1.326 ± 0.056	0.063 ± 0.012	0.0314 ± 0.0062	0.00387 ± 0.00028	0.00130 ± 0.00014	-0.05	24.9 ± 1.8	31.1 ± 6.1	26.3 ± 2.9
KH172-15c	0.789 ± 0.024	0.047 ± 0.024	0.025 ± 0.011	0.00397 ± 0.00037	0.00116 ± 0.00016	-0.26	25.5 ± 2.4	24 ± 11	23.5 ± 3.1
KH172-16	0.559 ± 0.019	0.0528 ± 0.0062	0.0283 ± 0.0034	0.00386 ± 0.00013	0.001269 ± 0.000054	0.16	24.83 ± 0.81	28.3 ± 3.3	25.6 ± 1.1
KH172-17	1.722 ± 0.064	0.058 ± 0.014	0.0335 ± 0.0087	0.00393 ± 0.00025	0.00142 ± 0.00020	0.10	25.3 ± 1.6	32.9 ± 8.4	28.6 ± 4.0
KH172-18-in	2.744 ± 0.098	0.117 ± 0.058	0.045 ± 0.022	0.00415 ± 0.00047	0.00311 ± 0.00082	0.17	26.7 ± 3.0	42 ± 21	63 ± 17
KH172-19	1.369 ± 0.046	0.0464 ± 0.0080	0.0259 ± 0.0046	0.00406 ± 0.00021	0.00144 ± 0.00013	0.27	26.1 ± 1.3	25.8 ± 4.5	29.1 ± 2.7
KH172-20	0.990 ± 0.044	0.0431 ± 0.0090	0.0230 ± 0.0047	0.00398 ± 0.00019	0.00140 ± 0.00011	0.02	25.6 ± 1.2	23.0 ± 4.6	28.4 ± 2.3
KH172-21c	2.36 ± 0.10	0.044 ± 0.015	0.030 ± 0.010	0.00398 ± 0.00035	0.00123 ± 0.00029	0.19	25.6 ± 2.2	29 ± 10	24.9 ± 5.9
KH172-22	1.087 ± 0.033	0.0392 ± 0.0078	0.0225 ± 0.0045	0.00406 ± 0.00015	0.001331 ± 0.000093	0.21	26.10 ± 0.97	22.4 ± 4.4	26.9 ± 1.9
KH172-23	1.255 ± 0.035	0.046 ± 0.011	0.0237 ± 0.0052	0.00402 ± 0.00021	0.00130 ± 0.00015	-0.12	25.8 ± 1.4	23.5 ± 5.1	26.2 ± 3.1
KH172-24	1.267 ± 0.037	0.0420 ± 0.0092	0.0223 ± 0.0046	0.00407 ± 0.00020	0.00122 ± 0.00011	0.17	26.2 ± 1.3	22.2 ± 4.5	24.6 ± 2.3
MN07; Dacite porphyry; 21.53 ± 0.35 Ma									
MN07-1	0.504 ± 0.037	0.165 ± 0.036	0.085 ± 0.023	0.00396 ± 0.00024	0.00191 ± 0.00027	0.66	25.5 ± 1.5	80 ± 19	38.6 ± 5.4
MN07-2	0.273 ± 0.011	0.784 ± 0.062	5.49 ± 0.79	0.0486 ± 0.0024	0.0278 ± 0.0014	0.21	306 ± 15	1860 ± 120	553 ± 28
MN07-3	0.829 ± 0.024	0.063 ± 0.011	0.0303 ± 0.0055	0.00340 ± 0.00016	0.001061 ± 0.000080	0.27	21.9 ± 1.0	30.1 ± 5.4	21.4 ± 1.6
MN07-4	1.001 ± 0.051	0.0611 ± 0.0096	0.0275 ± 0.0046	0.00342 ± 0.00019	0.00120 ± 0.00010	0.37	22.0 ± 1.2	27.5 ± 4.5	24.3 ± 2.1
MN07-5	1.109 ± 0.063	0.0408 ± 0.0086	0.0190 ± 0.0039	0.00348 ± 0.00015	0.001087 ± 0.000099	0.03	22.41 ± 0.99	19.0 ± 3.9	22.0 ± 2.0
MN07-6	0.841 ± 0.039	0.0467 ± 0.0094	0.0226 ± 0.0041	0.00366 ± 0.00023	0.001093 ± 0.000072	0.05	23.5 ± 1.5	22.6 ± 4.1	22.1 ± 1.5
MN07-7	1.197 ± 0.043	0.063 ± 0.012	0.0284 ± 0.0056	0.00330 ± 0.00017	0.00121 ± 0.00011	0.11	21.2 ± 1.1	28.2 ± 5.6	24.4 ± 2.1
MN07-8	1.626 ± 0.086	0.0468 ± 0.0026	0.0499 ± 0.0029	0.00728 ± 0.00024	0.00248 ± 0.00011	0.01	46.8 ± 1.5	49.4 ± 2.8	50.1 ± 2.1
MN07-9	1.002 ± 0.045	0.0520 ± 0.0087	0.0238 ± 0.0041	0.00331 ± 0.00013	0.001031 ± 0.000063	0.09	21.27 ± 0.84	23.8 ± 4.1	21.1 ± 1.4
MN07-10	1.24 ± 0.19	0.0725 ± 0.0088	0.0663 ± 0.0085	0.00643 ± 0.00022	0.00241 ± 0.00023	0.14	41.3 ± 1.4	64.9 ± 8.0	48.6 ± 4.6
MN07-11	0.990 ± 0.058	0.051 ± 0.011	0.0222 ± 0.0047	0.00341 ± 0.00014	0.001160 ± 0.000082	-0.14	21.94 ± 0.93	22.1 ± 4.6	23.4 ± 1.7
MN07-12	1.142 ± 0.037	0.100 ± 0.016	0.0485 ± 0.0076	0.00360 ± 0.00018	0.00181 ± 0.00021	-0.01	23.2 ± 1.2	47.8 ± 7.4	36.5 ± 4.1
MN07-13	0.990 ± 0.050	0.154 ± 0.033	0.084 ± 0.019	0.00386 ± 0.00026	0.00222 ± 0.00026	0.10	24.8 ± 1.7	80 ± 18	44.8 ± 5.2
MN07-14	1.172 ± 0.064	0.080 ± 0.011	0.0354 ± 0.0046	0.00327 ± 0.00015	0.00137 ± 0.00017	0.34	21.02 ± 0.99	35.2 ± 4.5	27.6 ± 3.5

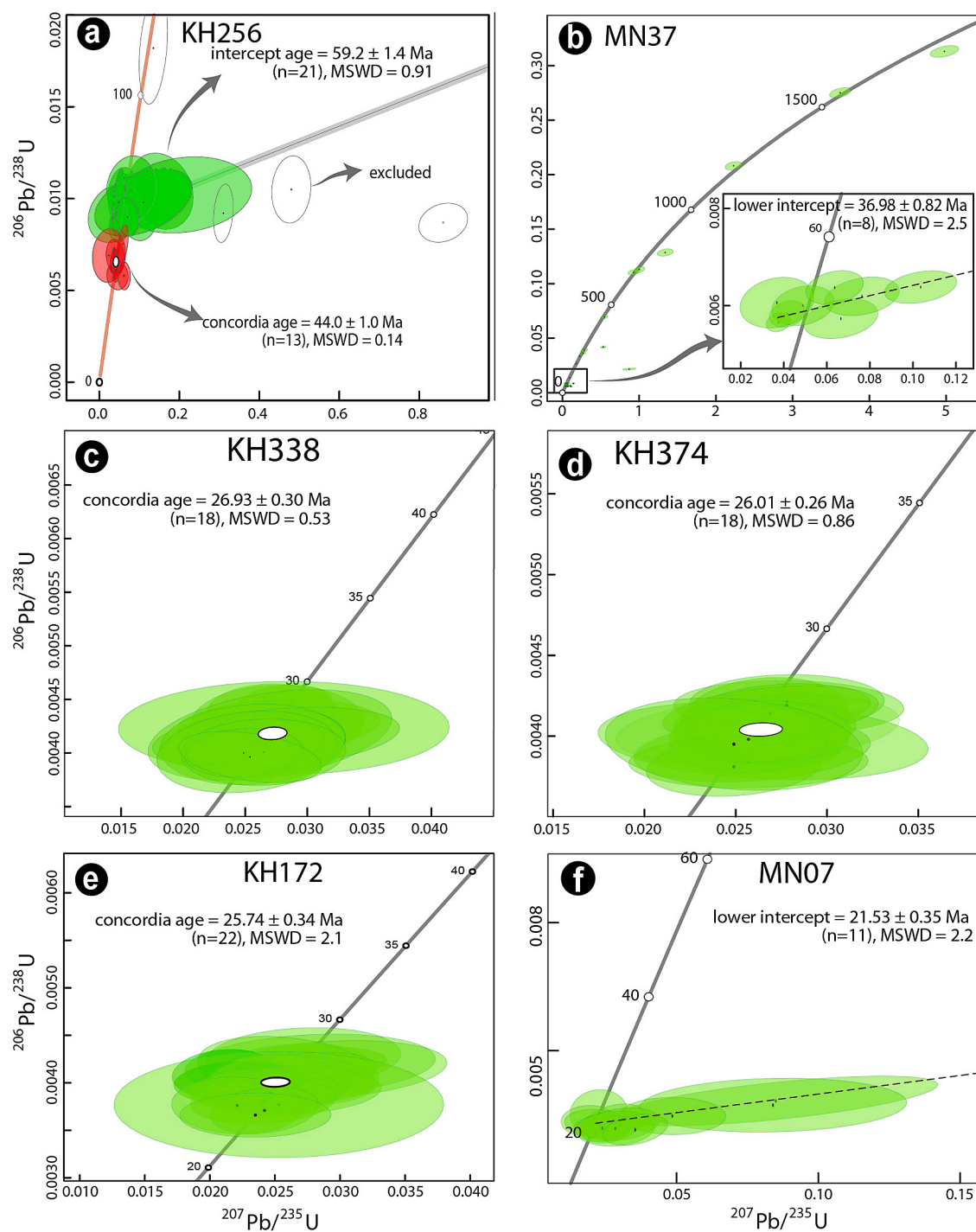


Fig. 7. Plots showing results of the LA-ICPMS zircon U-Pb age dating; Concordia ages (a, c-e) and intercept ages (b and f, which show evidence of Pb-loss). See also Table 3 for the corresponding analytical results.

Myr after the productive granodiorite porphyry body (Fig. 8c-d) and were less productive including blocks which are almost barren. Therefore, despite all the three Oligocene magma pulses in KHD show characteristics of productive magmas, such as adakitic signature and a similar REE pattern (Fig. 3c-d), the two younger magma batches are characterized by only minor Mo enrichments (91 and 45 ppm, respectively) and almost no Cu mineralization. However, the adakitic signature is more pronounced in the early granodiorite porphyry body than in the late granitic ones (Fig. 3c and Table 2). Such signature is documented by significantly higher $(La/Yb)_N$ and $(Dy/Yb)_N$ values and

slightly higher Sr/Y values than those obtained from the Eocene and early Miocene magmas. Whereas the $(La/Yb)_N$ and $(Dy/Yb)_N$ values attest that amphibole (\pm garnet) fractionation played the dominant role in magma differentiation (Klein et al., 1997; Davidson et al., 2007), the relatively low to moderate Sr/Y values, along with insignificant change in the Eu/Eu* values between Eocene and Oligocene magmas (Table 2), provide clear evidence that plagioclase was also a fractionating phase during the magma evolution (Taylor and McLennan, 1985; Defant and Drummond, 1990).

As dominant amphibole fractionation may occur in the lower crustal

Table 4

Synopsis of the Re-Os data for molybdenite.

Sample (KH256)	wt (g)	Re (ppm)	\pm	^{187}Re (ppm)	\pm	^{187}Os (ppb)	\pm	Age (Ma)	\pm (1)	\pm (2)	\pm (3)
RO1188-3.256.2.62	0.020	110.81	0.41	69.64	0.26	31.00	0.10	26.75	0.02	0.11	0.14

(1) Uncertainty including only spectrometry uncertainty.

(2) Uncertainty including all sources of analytical uncertainty.

(3) Uncertainty including all sources of analytical uncertainty plus decay constant.

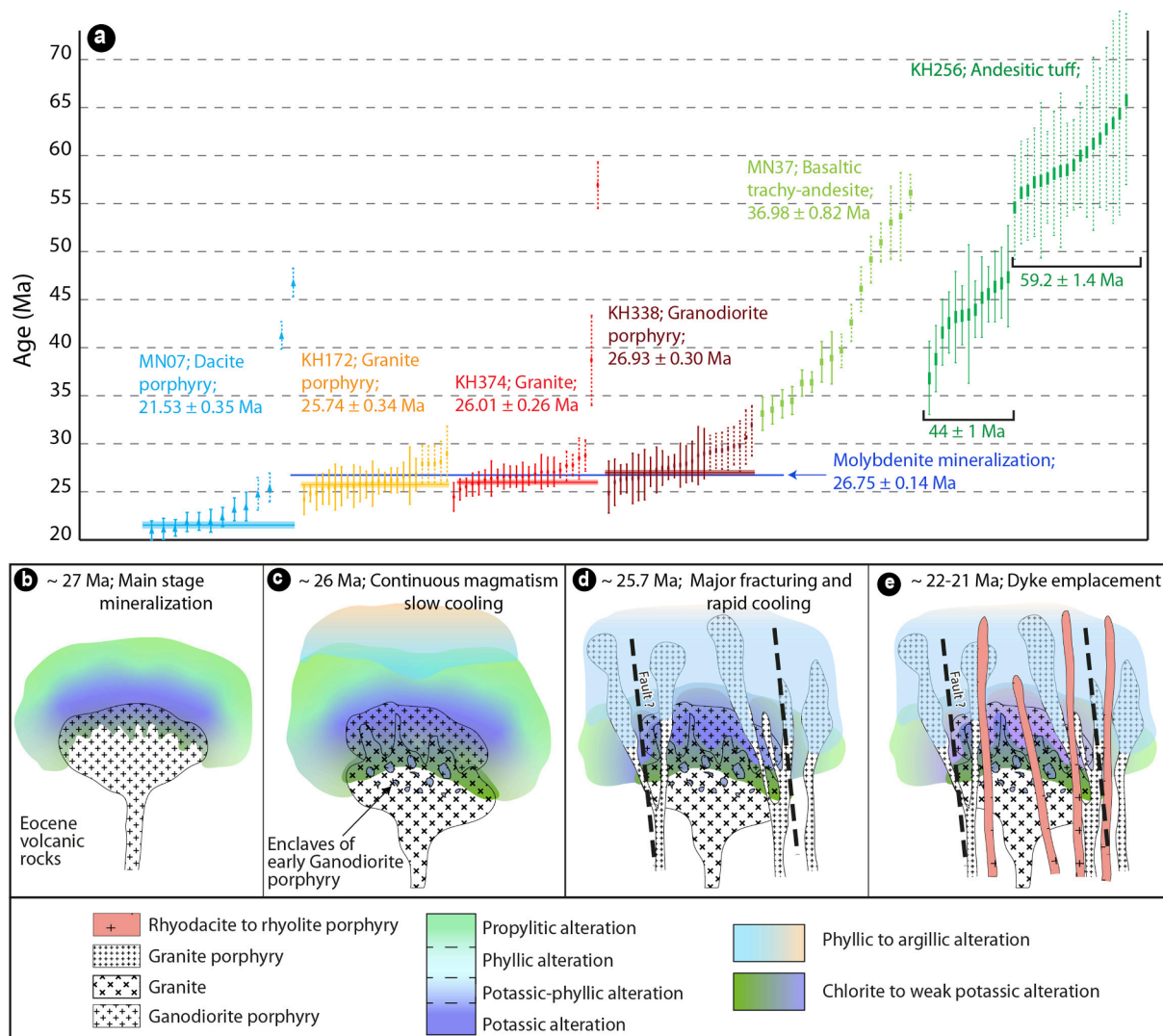


Fig. 8. (a) Distribution of all zircon U-Pb ages from KHD, including Eocene volcanic country rocks and Oligocene-early Miocene subvolcanic samples. The inherited zircons (pre-Cenozoic ages) are excluded from each zircon sample population. The ages are shown with 2σ uncertainty and the ones with dashed lines represent zircon antecrysts (Miller et al., 2007). (b-e) Conceptual models showing the sequential magma emplacement and the development of the hydrothermal system in KHD. From ~ 26 Ma, the new magmas were less productive to barren and consequently reduced the economic potential of the early-stage mineralization.

magma reservoirs in arc settings (e.g., Ducea and Saleeby, 1996; Sisson et al., 1996; Davidson et al., 2007; Larocque and Canil, 2010; Dessimoz et al., 2012; Rossetti et al., 2014), it was suggested that the water content of the magma was less than ~ 4 wt% to prevent plagioclase crystallization and generate a pronounced adakitic signature (Yoder, 1965; Gaetani et al., 1993; Sisson and Grove, 1993; Urann et al., 2022). A lower water content might indicate a relatively lower oxygen fugacity of the melt compared to those typically associated with porphyry Cu-Mo systems (e.g., Hamilton et al., 1964; Feig et al., 2010), hence, reducing the Cu enrichment in the porphyry system (e.g., Richards, 2011; Sun et al., 2014). Noteworthy, the $(\text{La}/\text{Yb})_{\text{N}}$ and $(\text{Dy}/\text{Yb})_{\text{N}}$ values

are lower in granite (~ 26 Ma; sample KH374), but significantly increase in the latest granodiorite porphyry (~ 25.7 Ma; sample KH172), suggesting a higher mineralization potential. However, the lower Sr/Y values in both these pulses of less mineralized magmas attests for an increased plagioclase fractionation.

We propose that these fractionation processes are not primarily due to changes in the magma feeding zone (likely at the lower crustal root); instead, they are more likely linked to physiochemical changes in the transcrustal magma system during crystallization and fluid exsolution within the mid-upper crustal magma chamber, ultimately influencing the magmatic-hydrothermal system(s) (Sillitoe, 2010; Richards, 2021).

In this regard appearance of a granular texture in the granite (sample KH374), after ~ 1 Myr from the emplacement of the early granodiorite porphyry, requires a lower cooling rate (passive fluid exsolution with no second boiling occurrence; Burnham, 1979; Candela, 1989) that likely was induced by a perturbed geothermal gradient during continuous magma emplacement at depth. In such conditions, fracturing is prevented and the mineralization more likely occurred only locally along the margins and roof of the stock, forming patchy mineralized zones and structurally controlled distal types, similar to the intrusion-related style (e.g., Lang and Baker, 2001; Rabiee, 2007). Indeed, a ~ 1 Myr time lapse is uncommon for a porphyry system which typically forms within 100,000 years or less (e.g., Shinohara and Hedenquist, 1997; Weis et al., 2012; Chiaradia et al., 2013; Chelle-Michou et al., 2017). It indicates that the Oligocene KHD mineralisation system did not experience a cumulative and rapid fluid exsolution compared to the lifespan of the magma underplating at depth (Richards, 2021). Example of the super-giant Chuquicamata porphyry Cu deposit resulted from a prolonged hydrothermal mineralization interval (>2.5 Myr), however, it is associated with two distinct, relatively rapid magma emplacement episodes separated by 0.5 Myr (Virmond et al., 2024). Furthermore, a magma accumulation and fluid exsolution period of ~ 1 Myr is inadequate to establish a sufficient flux of volatile- and metal-rich magma for subsequent granitic pulses (e.g., Chiaradia et al., 2009; Rabiee et al., 2022). In fact, despite a moderate to weak chlorite + pyrite alteration in this granite stock, only limited zones (few meters intervals) of low Mo and/or Cu enrichments are observed which most likely are related to the foundered fragments of the early mineralized granodiorite porphyry (Fig. 2g-h and 6 k). This inference is also supported by the observed telescopic mineralization of coexisting high- and low-temperature mineral assemblages (e.g., Mol + Ccp + TiO₂ vs Gb + Sp + Ba; Fig. 4g, 6a-l). The further emplacement of the latest Oligocene granite porphyry (sample KH172) was likely structurally controlled at shallower depths, causing rapid melt cooling, crystallization, and degassing, and hence, local fluid over-pressurization and stockwork veining. However, invasion of meteoric fluids, likely facilitated by continuous brittle fracturing. Consequently, formation of the early Kfs + Qz + Mol veins were minor whereas the type-D veins (phyllitic alteration) became dominant. The reported vast geochemically anomalous zones associated with phyllitic and silicic alterations (NICICO, 2010) can be thus explained by such brittle dominated environment that might have facilitated dispersion of the mineralizing fluids, enhanced by tendency of Mo to form complexes with OH migrating to peripheral zones (Xiaoyun, 1989; Ulrich and Mavrogenes, 2008). In this regard, the carbonatization documented in Khatoon-Abad has been also reported in the nearby Bashmaq IOCG-type (Sohrabi and Rezaei Aghdam, 2016) and Siah-Kamar Mo (Rabiee et al., 2023) porphyry deposits, was likely related to meteoric fluid infiltration and mixing with CO₂-bearing magmatic fluids facilitated by the progressive embrittlement of the caprocks sealing the hydrothermal system (Rabiee et al., 2019).

A major transition from productive to nonproductive magmas is documented with onset of the early Miocene magmatism (Fig. 3c), which caused a further degradation of the mineralising system at the KHD. Consequently, subsequent less-productive intrusions, along with the prevailing brittle condition and the invasion of the meteoric fluids diluted and dispersed the early segregated magmatic ones (e.g., Bouzari and Clark, 2006; Shinohara, 2008; Weis et al., 2012; Audébat and Li, 2017), and, ultimately, re-mobilized and devaluated the early-stage mineralization (e.g., Shinohara and Hedenquist, 1997).

5.3. Inferences for ore mineralization in collisional settings

The KHD is located between the neighbouring Siah-Kamar porphyry Mo (Nabatian et al., 2017; Rabiee et al., 2019) and the IOCG-type Bashmagh-Ghazikandi deposits (Sohrabi and Rezaei Aghdam, 2016) within the Mianeh-Hashtroud magmatic zone of the UDMA. The three deposits share a common genesis related to Oligocene felsic intrusions

with slightly variable emplacing times (Fig. 1 b). Although with different mineralisation characteristics, such productive magmas formed during the early stages of collisional thickening along the Arabia-Eurasia convergence zone, initiated around the late Eocene to early Oligocene in Armenia and NW-Iran (Agard et al., 2005; Ballato et al., 2011; Moritz et al., 2016; Rezeau et al., 2017; Rabiee et al., 2022). Significantly, the study area correspond to a region where orogen-parallel and orogen-transverse faults have interacted during the space-time evolution of the collisional tectonics along the UDMA (Fig. 1a; Barrier et al., 2018; 2021; Rabiee et al., 2020; 2022). By resolving the mineralisation type and characteristics of the Mianeh-Hashtroud magmatic zone we can thus infer how regional tectonics may impact on magmatism and associated mineralisation in collisional settings. In particular, when results of this study are integrated at regional scale, it is evident that the porphyry systems of similar Oligocene age along the UDMA are relatively small and low-grade (Rabiee et al., 2022). This evidence suggests that optimal conditions for porphyry mineralization were likely attenuated due to episodic tectonic disruptions, likely induced by polyphase fault reactivation during crustal shortening. Considering the duration of magma cooling, crystallization, mineralization and fluid exsolution events (Hedenquist and Lowenstern, 1994; Chelle-Michou et al., 2017), we suggest that short-term tectonic perturbations during continuous continental collision may affect (i) the physio-chemical conditions at the deposition site, and (ii) conditions of magma generation and transcrustal magma evolution and emplacement.

6. Conclusions

The most important findings arising from this study can be summarized as follows:

- The KHD formed within a long-lived and stationary zone of Tertiary magmatism, lasting at least 45 Myr, from ~ 66 to ~ 21 Ma. This prolonged and stationary magmatism funded the required ingredients to form productive magmas in Oligocene time (~ 27 – 25 Ma);
- The KHD mineralization began at ~ 27 Ma, followed and overprinted by less productive Oligocene and barren early Miocene magmatic pulses, spanning in age ~ 26 – 21 Ma;
- The late magma pulses degraded the economic potential of the early-generated ore body;
- Short-term tectonic changes in collisional settings can induce changes in the magma crystallization and fluid exsolution patterns (passive vs efficient), leading to different mineralization types/enrichments and fluid distribution (focused vs dispersed) during the transcrustal magma emplacement and deposition site.

Declaration of competing interest

The authors declare that they have no known competing financial interests or personal relationships that could have appeared to influence the work reported in this paper.

Acknowledgments

The grant to the Department of Science, Roma Tre University (MIUR-Italy Dipartimenti di Eccellenza, ARTICOLO 1, COMMI 314 – 337 LEGGE 232/2016) and the support of Rome Technopole (PNRR grant M4-C2-Inv) are gratefully acknowledged. We are indebted to K. Yamamoto for supporting and providing access to the LA-ICP-MS facilities at Nagoya University, and the support of Geoff Nowell and Chris Ottley at Durham University. Comments from two anonymous reviewers provided constructive comments that improved the manuscript.

Appendix A. Supplementary data

Supplementary data to this article can be found online at <https://doi.org/10.1016/j.oregeorev.2024.106330>.

Data availability

Data will be made available on request.

References

- Agard, P., Omrani, J., Jolivet, L., Moutheau, F., 2005. Convergence history across Zagros (Iran): constraints from collisional and earlier deformation. *Int. J. Earth Sci.* 94 (3), 401–419.
- Aghazadeh, M., Hou, Z., Badrzadeh, Z., Zhou, L., 2015. Temporal-spatial distribution and tectonic setting of porphyry copper deposits in Iran: Constraints from zircon U-Pb and molybdenite Re-Os geochronology. *Ore Geol. Rev.* 70, 385–406.
- Ahmadian, J., Sarjoughian, F., Lentz, D., Esna-Ashari, A., Murata, M., Ozawa, H., 2016. Eocene K-rich adakitic rocks in the Central Iran: implications for evaluating its Cu–Au–Mo metallogenic potential. *Ore Geol. Rev.* 72, 323–342.
- Alavi, M., 1994. Tectonics of the Zagros orogenic belt of Iran: new data and interpretations. *Tectonophysics* 229 (3–4), 211–238.
- Amidi, M., Alavi Tehrani, M., Lotfi, P., Haghipour, A., Sabzehei, M., Behroozi, A., Lescuyer, J., Riou, R., 1987. Geological map of Mianeh. Geological Survey of Iran, Tehran.
- Amidi, M., Lescuyer, J. and Riou, R., 1978. Ahar geological map in scale 1: 250,000. GSI.
- Asadi, S., 2018. Triggers for the generation of post-collisional porphyry Cu systems in the Kerman magmatic copper belt, Iran: New constraints from elemental and isotopic (Sr–Nd–Hf–O) data. *Gondw. Res.* 64, 97–121.
- Asadi, S., Moore, F., Zaravandi, A., 2014. Discriminating productive and barren porphyry copper deposits in the southeastern part of the central Iranian volcano-plutonic belt, Kerman region, Iran: a review. *Earth Sci. Rev.* 138, 25–46.
- Azizi, H., Stern, R.J., Topuz, G., Asahara, Y., Moghadam, H.S., 2019. Late Paleocene adakitic granitoid from NW Iran and comparison with adakites in the NE Turkey: Adakitic melt generation in normal continental crust. *Lithos* 346–347, 105151.
- Babazadeh, S., Furman, T., Santosh, M., Raeisi, D., Choi, S.H., D'Antonio, M., 2024a. Middle to Late Miocene K-rich magmatism in Central Iran: Geochemical characterization of the post-collision mantle beneath the Urumieh-Dokhtar magmatic arc. *Chem. Geol.* 665, 122308.
- Babazadeh, S., Ghalamghash, J., Raeisi, D., Santosh, M., Furman, T., Choi, S.H., D'Antonio, M., Heilimo, E., Cottle, J.M., 2024b. Arc magmatism associated with continental convergence in the SE segment of the UDMA, Iran: Insights from zircon geochronology and Hf–Sr–Nd–Fe isotopes. *Lithos* 466–467, 107468.
- Badr, M.J., Collins, A.S., Masoudi, F., Cox, G., Mohajel, M., 2013. The U–Pb age, geochemistry and tectonic significance of granitoids in the Soursat Complex, Northwest Iran. *Turk. J. Earth Sci.* 22 (1), 1–31.
- Ballato, P., Uba, C.E., Landgraf, A., Strecker, M.R., Sudo, M., Stockli, D.F., Friedrich, A., Tabatabaei, S.H., 2011. Arabia-Eurasia continental collision: insights from late Tertiary foreland-basin evolution in the Alborz Mountains, northern Iran. *Bulletin* 123 (1–2), 106–131.
- Ballato, P., Cifelli, F., Heidarzadeh, G., Ghassemi, M.R., Wickert, A.D., Hassanzadeh, J., Dupont-Nivet, G., Balling, P., Sudo, M., Zeilinger, G., 2017. Tectono-sedimentary evolution of the northern Iranian Plateau: insights from middle-late Miocene foreland-basin deposits. *Basin Res.* 29 (4), 417–446.
- Barra, F., Alcota, H., Rivera, S., Valencia, V., Munizaga, F., Maksaev, V., 2013. Timing and formation of porphyry Cu–Mo mineralization in the Chuquicamata district, northern Chile: new constraints from the Toki cluster. *Miner. Deposita* 48 (5), 629–651.
- Barrier, E., Vrielynck, B., Brouillet, J. and Brunet, M., 2018. Paleotectonic Reconstruction of the Central Tethyan Realm. Tectono-Sedimentary-Palinspastic maps from Late Permian to Pliocene. CCGM/CGMW, Paris. CCGM/CGMW Paris: France.
- Burnham, C.W., 1979. Magmas and hydrothermal fluids. *Geochemistry of Hydrothermal Ore Deposits*: 71–136.
- Candela, P., 1989. Magmatic ore-forming fluids: thermodynamic and mass-transfer calculations of metal concentrations. In ore deposition associated with magmas. *Rev. Econ. Geol.* 4, 203–221.
- Chelle-Michou, C., Rottier, B., Caricchi, L., Simpson, G., 2017. Tempo of magma degassing and the genesis of porphyry copper deposits. *Sci. Rep.* 7, 40566.
- Chen, Q., Wang, C., Bagas, L., Zhang, Z., Du, B., 2021. Time scales of multistage magma-related hydrothermal fluids at the giant Yulong porphyry Cu–Mo deposit in eastern Tibet: insights from titanium diffusion in quartz. *Ore Geol. Rev.* 139, 104459.
- Chiaradia, M., Caricchi, L., 2017. Stochastic modelling of deep magmatic controls on porphyry copper deposit endowment. *Sci. Rep.* 7, 44523.
- Chiaradia, M., Merino, D., Spikings, R., 2009. Rapid transition to long-lived deep crustal magmatic maturation and the formation of giant porphyry-related mineralization (Yanacocha, Peru). *Earth Planet. Sci. Lett.* 288 (3–4), 505–515.
- Chiaradia, M., Schaltegger, U., Spikings, R., Wotzlaw, J.-F., Ovtcharova, M., 2013. How accurately can we date the duration of magmatic-hydrothermal events in porphyry systems?—An invited paper. *Econ. Geol.* 108 (4), 565–584.
- G. Corbett Corbett, G., 2002. Structural controls to Porphyry Cu–Au and Epithermal Au–Ag deposits in. *Applied Structural Geology for Mineral Exploration*, Australian Institute of Geoscientists Bulletin, 36: 32–35.
- Courtney-Davies, L., Ciobanu, C.L., Tapster, S.R., Cook, N.J., Ehrig, K., Crowley, J.L., Verdugo-Ihl, M.R., Wade, B.P., Condon, D.J., 2020. Opening the magmatic-hydrothermal window: high-precision U–Pb geochronology of the mesoproterozoic Olympic dam Cu–U–Au–Ag deposit, south Australia. *Econ. Geol.* 115 (8), 1855–1870.
- Cox, S.F., Knackstedt, M.A. and Braun, J., 2001. Principles of Structural Control on Permeability and Fluid Flow in Hydrothermal Systems. In: J.P. Richards and R.M. Tosdal (Editors), *Structural Controls on Ore Genesis*. Society of Economic Geologists.
- Davidson, J., Turner, S., Handley, H., Macpherson, C., Dosseto, A., 2007. Amphibole “sponge” in arc crust? *Geology* 35 (9), 787–790.
- Defant, M.J., Drummond, M.S., 1990. Derivation of some modern arc magmas by melting of young subducted lithosphere. *Nature* 347 (6294), 662–665.
- Dessimoz, M., Müntener, O., Ulmer, P., 2012. A case for hornblende dominated fractionation of arc magmas: the Chelan Complex (Washington Cascades). *Contrib. Miner. Petrol.* 163 (4), 567–589.
- Ducea, M.N., Saleeby, J.B., 1996. Buoyancy sources for a large, unrooted mountain range, the Sierra Nevada, California: evidence from xenolith thermobarometry. *J. Geophys. Res. Solid Earth* 101 (B4), 8229–8244.
- Feig, S.T., Koepke, J., Snow, J.E., 2010. Effect of oxygen fugacity and water on phase equilibria of a hydrous tholeiitic basalt. *Contrib. Miner. Petrol.* 160 (4), 551–568.
- Gaetani, G.A., Grove, T.L., Bryan, W.B., 1993. The influence of water on the petrogenesis of subduction-related igneous rocks. *Nature* 365 (6444), 332–334.
- Ghorbani, M., 2021. The geology of Iran: tectonic, magmatism and metamorphism. Springer.
- Hamilton, D.L., Burnham, C.W., Osborn, E.F., 1964. The solubility of water and effects of oxygen fugacity and water content on crystallization in mafic magmas. *J. Petrol.* 5 (1), 21–39.
- Hassanpour, S., Alirezai, S., Selby, D., Sergeev, S., 2014. SHRIMP zircon U–Pb and biotite and hornblende Ar–Ar geochronology of Sungun, Haftcheshmeh, Kighal, and Niaz porphyry Cu–Mo systems: evidence for an early Miocene porphyry-style mineralization in northwest Iran. *Int. J. Earth Sci.* 104 (1), 45–59.
- Hassanzadeh, J., 1993. Metallogenic and tectono-magmatic events in the SE sector of the Cenozoic active continental margin of Iran (Shahr-e-Babak area, Kerman province). (Ph. D. Thesis). University of California.
- Hastie, A.R., Kerr, A.C., Pearce, J.A., Mitchell, S.F., 2007. Classification of altered volcanic island arc rocks using immobile trace elements: development of the Th–Co discrimination diagram. *J. Petrol.* 48 (12), 2341–2357.
- Hedenquist, J.W., Lowenstern, J.B., 1994. The role of magmas in the formation of hydrothermal ore deposits. *Nature* 370 (6490), 519.
- Hou, Z., Yang, Z., Qu, X., Meng, X., Li, Z., Beaudoin, G., Rui, Z., Gao, Y., Zaw, K., 2009. The Miocene Gangdese porphyry copper belt generated during post-collisional extension in the Tibetan Orogen. *Ore Geol. Rev.* 36 (1), 25–51.
- Karimpour, M.H., Malekzadeh Shafaroudi, A., Mazloumi Bajestani, A., Schader, R.K., Stern, C.R., Farmer, L., Sadeghi, M., 2017. Geochemistry, geochronology, isotope and fluid inclusion studies of the Kuh-e-Zar deposit, Khaf-Kashmar-Bardaskan magmatic belt, NE Iran: Evidence of gold-rich iron oxide–copper–gold deposit. *J. Geochem. Explor.* 183, 58–78.
- Khodabandeh, A.A., Amini Azar, R., Faridi, M., 1999. Geological map of the Mianeh quadrangle. Geological Survey of Iran and Mining Exploration, Tehran.
- Kirkland, C., Smithies, R., Taylor, R., Evans, N., McDonald, B., 2015. Zircon Th/U ratios in magmatic environments. *Lithos* 212, 397–414.
- Klein, M., Stosch, H.G., Seck, H.A., 1997. Partitioning of high field-strength and rare-earth elements between amphibole and quartz-dioritic to tonalitic melts: an experimental study. *Chem. Geol.* 138 (3), 257–271.
- Lang, J.R., Baker, T., 2001. Intrusion-related gold systems: the present level of understanding. *Miner. Deposita* 36 (6), 477–489.
- Large, S.J.E., Wotzlaw, J.F., Guillong, M., von Quadt, A., Heinrich, C.A., 2020. Resolving the timescales of magmatic and hydrothermal processes associated with porphyry deposit formation using zircon U–Pb petrochronology. *Geochronology* 2 (2), 209–230.
- Larocque, J., Canil, D., 2010. The role of amphibole in the evolution of arc magmas and crust: the case from the Jurassic Bonanza arc section, Vancouver Island, Canada. *Contribut. Mineral. Petrol.* 159 (4), 475–492.
- Le Maître, R.W., Streckenbach, A., Zanettin, B., Le Bas, M., Bonin, B., Bateman, P., 2005. Igneous rocks: a classification and glossary of terms: recommendations of the International Union of Geological Sciences Subcommission on the Systematics of Igneous Rocks. Cambridge University Press.
- Lee, C.-T.-A., Tang, M., 2020. How to make porphyry copper deposits. *Earth Planet. Sci. Lett.* 529, 115868.
- Loucks, R.R., 2014. Distinctive composition of copper-ore-forming arcmagmas. *Aust. J. Earth Sci.* 61 (1), 5–16.
- Martin, H., 1987. Petrogenesis of archaean trondhjemites, tonalites, and granodiorites from eastern Finland: major and trace element geochemistry. *J. Petrol.* 28 (5), 921–953.
- Middlemost, E.A., 1994. Naming materials in the magma/igneous rock system. *Earth Sci. Rev.* 37 (3–4), 215–224.
- Miller, J.S., Matzel, J.E.P., Miller, C.F., Burgess, S.D., Miller, R.B., 2007. Zircon growth and recycling during the assembly of large, composite arc plutons. *J. Volcanol. Geoth. Res.* 167 (1), 282–299.
- Moritz, R., Ghazban, F., Singer, B.S., 2006. Eocene gold ore formation at Muteh, Sanandaj-Sirjan tectonic zone, Western Iran: a result of late-stage extension and exhumation of metamorphic basement rocks within the Zagros Orogen. *Econ. Geol.* 101 (8), 1497–1524.
- Moritz, R., Rezeau, H., Ovtcharova, M., Tayan, R., Melkonyan, R., Hovakimyan, S., Ramazanov, V., Selby, D., Ulianov, A., Chiaradia, M., 2016. Long-lived, stationary magmatism and pulsed porphyry systems during Tethyan subduction to post-

- collision evolution in the southernmost Lesser Caucasus, Armenia and Nakhitchevan. *Gondw. Res.* 37, 465–503.
- Nabatian, G., Wan, B., Honarmand, M., 2017. Whole rock geochemistry, molybdenite Re-Os geochronology, stable isotope and fluid inclusion investigations of the Siah-Kamar deposit, western Alborz-Azbarayjan: New constrains on the porphyry Mo deposit in Iran. *Ore Geol. Rev.* 91, 638–659.
- NICICO, 2009a. Geological report and map of Goydaraq area, at scale of 1:25000, Internal report.
- NICICO, 2009b. Geological report and map of Khatoon-Abad area, at scale of 1:25000, Internal report.
- NICICO, 2009c. Geological report and map of Siah-Kamar area, at scale of 1:25000, Internal report.
- NICICO, 2010. Geological report and map of Khatoon Abad area, at scale of 1:5000, Internal report.
- Oyarzun, R., Márquez, A., Lillo, J., López, I., Rivera, S., 2001. Giant versus small porphyry copper deposits of Cenozoic age in northern Chile: adakitic versus normal calc-alkaline magmatism. *Miner. Deposita* 36 (8), 794–798.
- Palme, H. and O'Neill, H.S.C., 2014. 3.1 Cosmochemical estimates of mantle composition, Treatise on Geochemistry: Oxford. Elsevier, pp. 1–39.
- Rabiee, A., Rossetti, F., Tecce, F., Asahara, Y., Azizi, H., Gladny, J., Lucci, F., Nozaem, R., Opitz, J., Selby, D., 2019. Multiphase magma intrusion, ore-enhancement and hydrothermal carbonatisation in the Siah-Kamar porphyry Mo deposit, Urumieh-Dokhtar magmatic zone, NW Iran. *Ore Geol. Rev.* 110, 102930.
- Rabiee, A., Rossetti, F., Asahara, Y., Azizi, H., Lucci, F., Lustrino, M., Nozaem, R., 2020. Long-lived, Eocene-Miocene stationary magmatism in NW Iran along a transform plate boundary. *Gondw. Res.* 85, 237–262.
- Rabiee, A., Rossetti, F., Lucci, F., Lustrino, M., 2022. Cenozoic porphyry and other hydrothermal ore deposits along the South Caucasus-West Iranian tectono-magmatic belt: A critical reappraisal of the controlling factors. *Lithos* 430–431, 106874.
- Rabiee, A., Rossetti, F., Asahara, Y., Azizi, H., Rajabinasab, B., Brilli, M., Atudorei, N.-V., Lucci, F., 2023. Carbonatisation and overprinting mineralisation in Siah-Kamar porphyry molybdenum deposit, NW Iran. *J. Geochem. Explor.* 251, 107230.
- Rabiee, A., 2007. Geochemical exploration of the Kuh-e Dom area and genesis of the Kuh-e Dom gold prospect, MSc Thesis (in Persian). Tarbiat Moalem University of Tehran, Iran, pp. 172.
- Rezeau, H., Moritz, R., Wotzlaw, J.-F., Tayan, R., Melkonyan, R., Ulianov, A., Selby, D., d'Abzac, F.-X., Stern, R.A., 2016. Temporal and genetic link between incremental pluton assembly and pulsed porphyry Cu-Mo formation in accretionary orogens. *Geology* 44 (8), 627–630.
- Rezeau, H., Moritz, R., Leuthold, J., Hovakimyan, S., Tayan, R., Chiaradia, M., 2017. 30 Myr of Cenozoic magmatism along the Tethyan margin during Arabia-Eurasia accretionary orogenesis (Meghri-Ordubad pluton, southernmost Lesser Caucasus). *Lithos* 288–289, 108–124.
- Richards, J.P., 2011. High Sr/Y arc magmas and porphyry Cu±Mo±Au deposits: just add water. *Econ. Geol.* 106 (7), 1075–1081.
- Richards, J.P., 2021. Porphyry copper deposit formation in arcs: What are the odds? *Geosphere* 18 (1), 130–155.
- Richards, J.P., Razavi, A.M., Spell, T.L., Locock, A., Sholeh, A., Aghazadeh, M., 2018. Magmatic evolution and porphyry–epithermal mineralization in the Taftan volcanic complex, southeastern Iran. *Ore Geol. Rev.* 95, 258–279.
- Richards, J., 2000. Lineaments revisited. *SEG newsletter*, 42(1): 14–20.
- Rossetti, F., Nasrabad, M., Theye, T., Gerdes, A., Monié, P., Lucci, F., Vignaroli, G., 2014. Adakite differentiation and emplacement in a subduction channel: the late Paleocene Sabzevar magmatism (NE Iran). *GSA Bull.* 126 (3–4), 317–343.
- Rubatto, D., 2002. Zircon trace element geochemistry: partitioning with garnet and the link between U-Pb ages and metamorphism. *Chem. Geol.* 184 (1–2), 123–138.
- Shafiei, B., Shahabpour, J., Haschke, M., 2008. Transition from Paleogene normal calc-alkaline to Neogene adakitic-like plutonism and Cu-metallogenesis in the Kerman porphyry copper belt: response to Neogene crustal thickening. *J. Sci., Islamic Repub. Iran* 19 (1), 67–84.
- Shafiei, B., Haschke, M., Shahabpour, J., 2009. Recycling of orogenic arc crust triggers porphyry Cu mineralization in Kerman Cenozoic arc rocks, southeastern Iran. *Miner. Deposita* 44 (3), 265.
- Shahabpour, J., Kramers, J., 1987. Lead isotope data from the Sar-Cheshmeh porphyry copper deposit. *Iran. Mineralium Deposita* 22 (4), 278–281.
- Shinohara, H., Hedenquist, J.W., 1997. Constraints on magma degassing beneath the far Southeast Porphyry Cu-Au deposit, Philippines. *J. Petrol.* 38 (12), 1741–1752.
- Siani, M.G., Mehrabi, B., Azizi, H., Wilkinson, C.M., Ganerod, M., 2015. Geochemistry and geochronology of the volcano-plutonic rocks associated with the Glojeh epithermal gold mineralization, NW Iran. *Open Geosci.* 7 (1).
- Sillitoe, R.H., 2010. Porphyry copper systems. *Economic geology*, 105(1): 3–41.
- Simmonds, V., Moazzem, M., Selby, D., 2019. U-Pb zircon and Re-Os molybdenite age of the Siah Kamar porphyry molybdenum deposit, NW Iran. *Int. Geol. Rev.* 61, 1786–17802.
- Sisson, T.W., Grove, T.L., 1993. Experimental investigations of the role of H₂O in calc-alkaline differentiation and subduction zone magmatism. *Contrib. Miner. Petrol.* 113 (2), 143–166.
- Sisson, T.W., Grove, T.L., Coleman, D.S., 1996. Hornblende gabbro sill complex at Onion Valley, California, and a mixing origin for the Sierra Nevada batholith. *Contrib. Miner. Petrol.* 126 (1), 81–108.
- Sohrabi, G. and Rezaei Aghdam, M., 2016. IOCG Mineralization in Bostanabad- Meyaneh metallogenic zone (NE Hashtrud), 34th National & 2nd International Geosciences Congress, Tehran, Iran.
- Sun, W.-D., Huang, R.-F., Liang, H.-Y., Ling, M.-X., Li, C.-Y., Ding, X., Zhang, H., Yang, X.-Y., Ireland, T., Fan, W.-M., 2014. Magnetite-hematite, oxygen fugacity, adakite and porphyry copper deposits: Reply to Richards. *Geochim. Cosmochim. Acta* 126, 646–649.
- Sun, S.S., McDonough, W.F., 1989. Chemical and isotopic systematics of oceanic basalts: implications for mantle composition and processes. *Geol. Soc. Lond. Spec. Publ.* 42 (1), 313–345.
- Taghipour, N., Aftabi, A., Mathur, R., 2008. Geology and Re-Os geochronology of mineralization of the miduk porphyry copper deposit, Iran. *Resour. Geol.* 58 (2), 143–160.
- Taylor, S.R., McLennan, S.M., 1985. The continental crust: Its composition and evolution. Blackwell Scientific Pub, Palo Alto, CA, United States.
- Tosdal, R., 2001. Magmatic and structural controls on the development of porphyry Cu±Mo±Au deposits. *Rev. in Econ. Geol.* 14, 157–181.
- Ulrich, T., Heinrich, C.A., 2002. Geology and alteration geochemistry of the porphyry Cu-Au deposit at Bajo de la Alumbra, Argentina. *Econ. Geol.* 97 (8), 1865–1888.
- Ulrich, T., Mavrogenes, J., 2008. An experimental study of the solubility of molybdenum in H₂O and KCl-H₂O solutions from 500°C to 800°C, and 150 to 300MPa. *Geochim. Cosmochim. Acta* 72 (9), 2316–2330.
- Urran, B.M., Le Roux, V., Jagoutz, O., Müntener, O., Behn, M.D., Chin, E.J., 2022. High water content of arc magmas recorded in cumulates from subduction zone lower crust. *Nat. Geosci.* 15 (6), 501–508.
- Virmond, A.L., Wotzlaw, J.-F., Arancibia, R.R., Selby, D. and Chelle-Michou, C., 2024. Multi-million-year magmatic and hydrothermal activity is key to the formation of supergiant to behemothian porphyry copper deposits Contributions to Mineralogy and Petrology.
- Vry, V.H., Wilkinson, J.J., Seguel, J., Millán, J., 2010. Multistage Intrusion, Brecciation, and Veining at El Teniente, Chile: Evolution of a Nested Porphyry System. *Econ. Geol.* 105 (1), 119–153.
- Weis, P., Driesner, T., Heinrich, C.A., 2012. Porphyry-copper ore shells form at stable pressure-temperature fronts within dynamic fluid plumes. *Science* 338 (6114), 1613–1616.
- Whitney, D.L., Evans, B.W., 2010. Abbreviations for names of rock-forming minerals. *Am. Mineral.* 95 (1), 185–187.
- Wilkinson, J.J., 2013. Triggers for the formation of porphyry ore deposits in magmatic arcs. *Nat. Geosci.* 6 (11), 917–925.
- Xiaoyun, C., 1989. Solubility of molybdenite and the transport of molybdenum in hydrothermal solutions. Ph. D. thesis. Iowa State University, 1~111.
- Xue, C., Chi, G., Zhao, X., Wu, G., Zhao, Z., Dong, L., 2016. Multiple and prolonged porphyry Cu-Au mineralization and alteration events in the Halasu deposit, Chinese Altai, Xinjiang, northwestern China. *Geosci. Front.* 7 (5), 799–809.
- Yang, Z., Zhang, X.-F., 2021. Multiphase intrusion at the giant Pulang porphyry Cu-Au deposit in western Yunnan (Southwestern China): comparison between ore-causative and barren intrusions. *Mineral. Petrol.* 115 (2), 223–240.
- Yoder, H., 1965. Diopside-anorthite-water at five and ten kilobars and its bearing on explosive volcanism. Carnegie Institution of Washington Yearbook, 64: 82–89.

References in supplementary materials

- Chew, D.M., Petrus, J.A., Kamber, B.S., 2014. U-Pb LA-ICPMS dating using accessory mineral standards with variable common Pb. *Chemical Geology* 363, 185–199.
- Gündüz, M., Asan, K., 2021. PetroGram: An excel-based petrology program for modeling of magmatic processes. *Geoscience Frontiers* 12 (1), 81–92.
- Iwano, H., Orihashi, Y., Hirata, T., Ogasawara, M., Danhara, T., Horie, K., Hasebe, N., Sueoka, S., Tamura, A., Hayasaka, Y., 2013. An inter-laboratory evaluation of OD-3 zircon for use as a secondary U-Pb dating standard. *Island Arc* 22 (3), 382–394.
- Paton, C., Hellstrom, J., Paul, B., Woodhead, J., Hergt, J., 2011. Iolite: Freeware for the visualisation and processing of mass spectrometric data. *Journal of Analytical Atomic Spectrometry* 26 (12), 2508–2518.
- Petrus, J.A., Kamber, B.S., 2012. VizualAge: A Novel Approach to Laser Ablation ICP-MS U-Pb Geochronology Data Reduction. *Geostandards and Geoanalytical Research* 36 (3), 247–270.
- Selby, D., Creaser, R.A., 2004. Macroscale NTIMS and microscale LA-MC-ICP-MS Re-Os isotopic analysis of molybdenite: Testing spatial restrictions for reliable Re-Os age determinations, and implications for the decoupling of Re and Os within molybdenite. *Geochimica et Cosmochimica Acta* 68 (19), 3897–3908.
- Sláma, J., Košler, J., Condon, D.J., Crowley, J.L., Gerdes, A., Hanchar, J.M., Horstwood, M.S.A., Morris, G.A., Nasdala, L., Norberg, N., Schaltegger, U., Schoene, B., Tubrett, M.N., Whitehouse, M.J., 2008. Plešovice zircon — A new natural reference material for U-Pb and Hf isotopic microanalysis. *Chemical Geology* 249 (1), 1–35.
- Smoliar, M.I., Walker, R.J., Morgan, J.W., 1996. Re-Os ages of group IIa, IIIa, IVA, and IVB iron meteorites. *Science* 271 (5252), 1099–1102.
- Stacey, J.t., Kramers, J., 1975. Approximation of terrestrial lead isotope evolution by a two-stage model. *Earth and planetary science letters* 26 (2), 207–221.
- Vermeesch, P., 2018. IsoplotR: A free and open toolbox for geochronology. *Geoscience Frontiers* 9 (5), 1479–1493.
- Wiedenbeck, M., Alle, P., Corfu, F., Griffin, W., Meier, M., Oberli, F.v., Quadt, A.v., Roddick, J., Spiegel, W., 1995. Three natural zircon standards for U-Th-Pb, Lu-Hf, trace element and REE analyses. *Geostandards newsletter* 19 (1), 1–23.